東京大学　大学院新領域創成科学研究科
基盤科学研究系
先端エネルギー工学専攻

平成18年度
修士論文

Electron Density Distribution Behind a Laser Supported Detonation Wave

レーザー支持爆轟波背後の電子密度分布

2007年2月提出
指導教員　小紫　公也　助教授

56208　河村　好一

Contents

List of Figures

List of Tables

Acknowledgments

I would like to extend my deepest gratitude to Professor Kimiya Komurasaki (Department of Advanced Energy, University of Tokyo) for his supervision and advisement. My master’s thesis couldn’t be completed without his steady instruction.

I would like to extend thanks to Professor Yoshihiro Arakawa (Department of Aeronautics and Astronautics, University of Tokyo)

I would like to express my appreciation to Mr. Masato Ushio. He taught me how to use experimental apparatus and forward experiments. In addition, he advised me constructive thinking that is necessary to research. This thinking will be of substantial aid in my life.

I gave my thanks to Mr. Fukui and Mr. Hatai. They supported my research. I earnestly hope that they will have such a fulfilling times, fulfilling discussion and fulfilling results.

I would like to express my appreciation to Mr. Hiroyuki Koizumi, Mr. Makoto Matsui, Mr. Takayoshi Inoue, Mr. Hiroki Takayanagi, Mr. Yasuhisa Oda and Mr. Shigeru Yokota for providing their helps, advices and kindness.

I wish to thank all members Arakawa and Komurasaki laboratories, especially I acknowledgements to the members in Kashiwa. I hope that their will maintain a better environment for their researches.

Finally, I would like to extend my gratitude to my family and familiar person for financial, mental and tremendous helps.

Chapter 1

Introduction

1.1 Laser propulsion

Laser propulsion is a candidate for a low cost and less fuel launching system. And this propulsion can be considered as the mass driver, in which the vehicle is accelerated by the laser power transmitted remotely from the ground-based laser oscillator. Kantrovitz first proposed laser propulsion in 1972 soon after the invention of laser[1]. To his proposal, many studies on the laser propulsion were activated especially in U.S.A, Russia and Japan. Especially Mylado carried out and succeeded the demonstration of the flight of the pulse laser propulsion at height about 70 meters.

Laser propulsion uses laser energy to thrust, which is very different from the conventional chemical rocket. This propulsion has big advantage over conventional chemical propulsion. Laser propulsion is classified into the following two modes according to the laser transmission mode.

CW laser propulsion Continuous wave (CW) laser propulsion uses the continuous wave laser. CW laser beam focused in the engines. Laser Sustained Plasma (LSP) is generated on the focus. LSP is maintained by the laser energy absorption through the inverse bremsstrahlung process. LSP supplies its enthalpy to the cold propellant gas, which flows around LSP. The heated propellant gas passes through the throat and expands in the nozzle. In this expansion stage, the gained enthalpy is converted into the kinetic energy. In this way, thrust is provided.

CW laser propulsion is considered to be applied to transitions between the orbits and the attitude control in the space because the CW laser, which power is presently several KW class, is not enough to launch the vehicles from the ground. Applying CW laser propulsion in the space has the advantages that propellant gases could be selected freely.

RP laser propulsion Repetitively Pulsed (RP) laser propulsion uses the repetitively pulsed laser. Pulse laser beam focused in the ablator on board or in the air. Then laser-induced plasma and blast wave is generated on the focus. The plasma supports the blast wave. This particular kind blast wave is called Laser supported detonation (LSD) wave. The flow energy converts into the thrust. The detail of this process and LSD wave is described later section.

RP laser propulsion is considered to be applied to the ground launch system because the RP laser, which power is presently several MW class. By comparison with the chemical rocket, applying RP laser propulsion to ground launch system has the advantages that there is no need to be the complex and heavy propulsion systems on board because laser energy is transmitted from the base located in the space or on the ground.

This study is drawn attention on RP laser propulsion and LSD wave. In particular this study is focused on the clear up of the phenomena of LSD.

1.2 RP laser propulsion

From the 70 's through 80 's, many studies were performed for the flat-plate type [2][3][4][5]. An intense laser beam was irradiated on a metallic plate surface in the atmospheric air to produce a high-pressure region on the surface as illustrated in Fig.1.1(a)[6]. Pirri et al. first studied a laser pulsejet with a bell nozzle illustrated in Fig.1.1(b). A laser beam was focused by a parabolic mirror to produce plasma. Expansion of the plasma drives a spherical blast wave in the surrounding air, and impulsive thrust is generated on the nozzle wall while the blast wave expands in the nozzle.

Ageev et al. also studied a laser pulsejet experimentally using a parabola and conical nozzle with a 5J-pulse CO2 laser [7]. In DLR (German Aerospace Center), a 53g-Bell nozzle was launched to 60cm high using a repetitive pulse laser whose average power was 7.9 KW (the laser pulse energy was 175J/pulse and the repetition frequency was 45 Hz) [8].

In 1998, Myrabo et al. published the results of their flight demonstrations using a 10kW-class repetitive pulse CO2 laser [9]. Their demonstrations were the world first and recent researches on laser propulsion were activated by their report. A ‘ Lightcraft ’ used in the demonstrations is illustrated in Fig.1.1(c). An impulsive thrust is imparted on a spike nozzle, which focuses a laser beam onto a cowl to produce plasma. Its mechanisms of impulse generation are same with those in the laser pulsejet though the geometry of focusing optics is different from the Bell type nozzle. One remarkable feature of the Lightcraft design is a front intake from which the air is taken and compressed.

A Laser In-Tube Accelerator (LITA) [10] is another variety of laser propulsion. LITA is a laser-driven ram accelerator where a projectile is accelerated by successive laser-induced explosions in a tube filled with a rare gas. Its thrust generation mechanisms are also quite similar to those of the laser pulsejet.

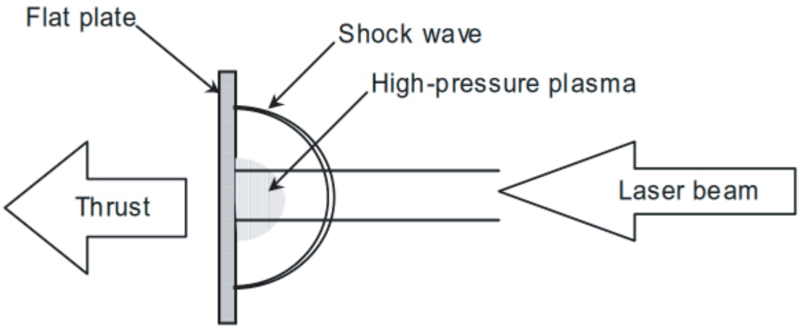

(a) Flat plate type laser propulsion

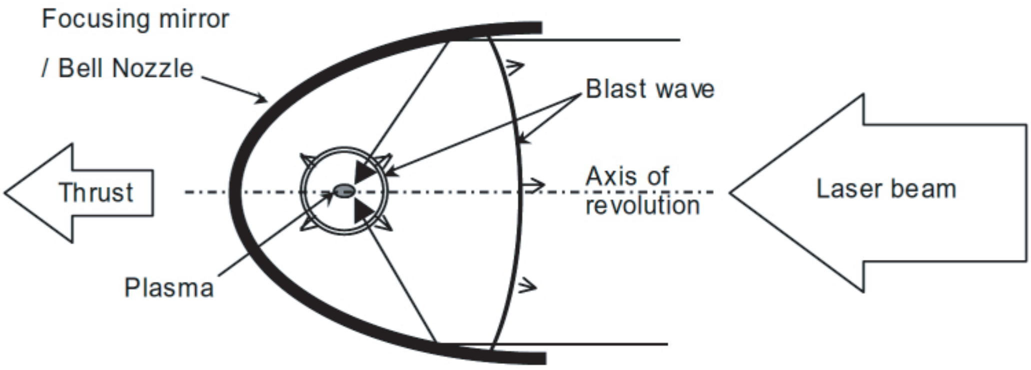

(b) Laser pulsejet with a Bell nozzle

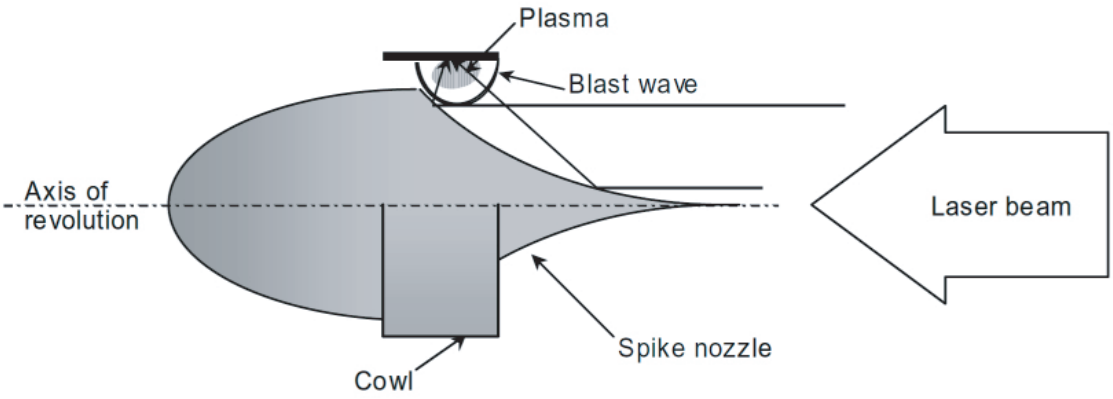

(c) Lightcraft designed by Myrabo

Figure 1.1: Schematics of differnet varieties of the propulsion

1.3 Our vision of the RP laser propulsion

Laser-Powered launch system would be the material supply for the construction of a Solar Power Satellite, for example. Our perspective of launch is introduced here to survey the overall picture of the system. Payload is launched through three modes; pulsejet, ramjet and rocket, as shown in Fig.1.2 Near the ground, the vehicle is accelerated until the velocity of the vehicle reach to M=2. This mode is called pulsejet mode. When the velocity of the vehicle reach to M=2, the air intake open and the air is drawn in at the front of the vehicle and compressed to compensate the reduction of the ambient pressure. This mode is called ramjet mode. In ramjet mode, compared to the pulsejet mode, the time to exhaust and refill air in the nozzle is much shorter because the intake flesh air sweep away the high-temperature and low-pressure air toward the rearward of the vehicle. Therefore, compared to the pulsejet mode, the laser pulse could send to the vehicle with high frequency in the ramjet mode. The rocket mode is initiated at the altitude where the adequate air pressure can not be acquired through the ram compression. In the rocket mode, the hydrogen on board is injected into the nozzle is injected into the nozzle with the pressure of the propellant tank higher than the pressure of the nozzle, and used as the working fluid.

The velocity increment by the laser propulsion at 10 km/s is required to launch a payload to GEO. An engine cycle analysis was adapted to the estimation of the thrust performance, and the specifications of the engine model are summarized in Table.1.1 Fig.1.3 shows the vehicle trajectory calculated by Katsurayama et al. for the vertical launch [11]. A vehicle is gradually accelerated through a trajectory from the sea-level up to 200km above sea level, and it will not suffer from excessive aerodynamic heating and load. A 100kg-vehicle accelerated to 10km/s in one minute, and the payload ratio of the vehicle was 0.6.

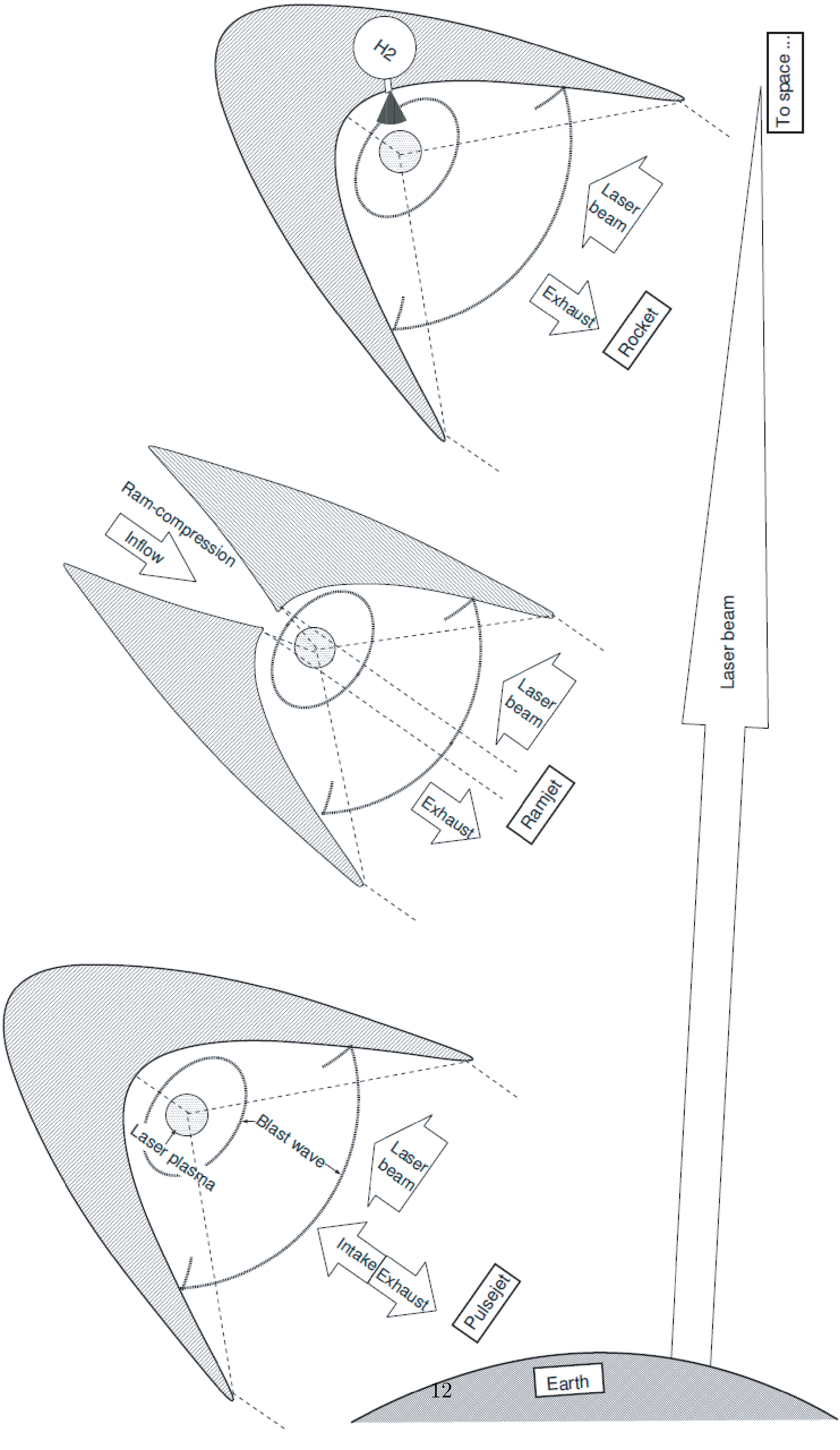

Figure 1.2: 3modes of the laser propulsion launch system

Table 1.1: The specifications of the engine model

Transmitted Laser	Average power (MW)	500
Vehicle	Initial mass (kg)	100
	Structure coefficient	0.1
Pulsejet mode	Cm (N/MW)	100
Ramjet mode	Absorption efficiency (%)	40
	Diffuser efficiency (%)	97
Rocket mode	Absorption efficiency (%)	40
	Propellant	H^2
	Specific impulse (s)	~950

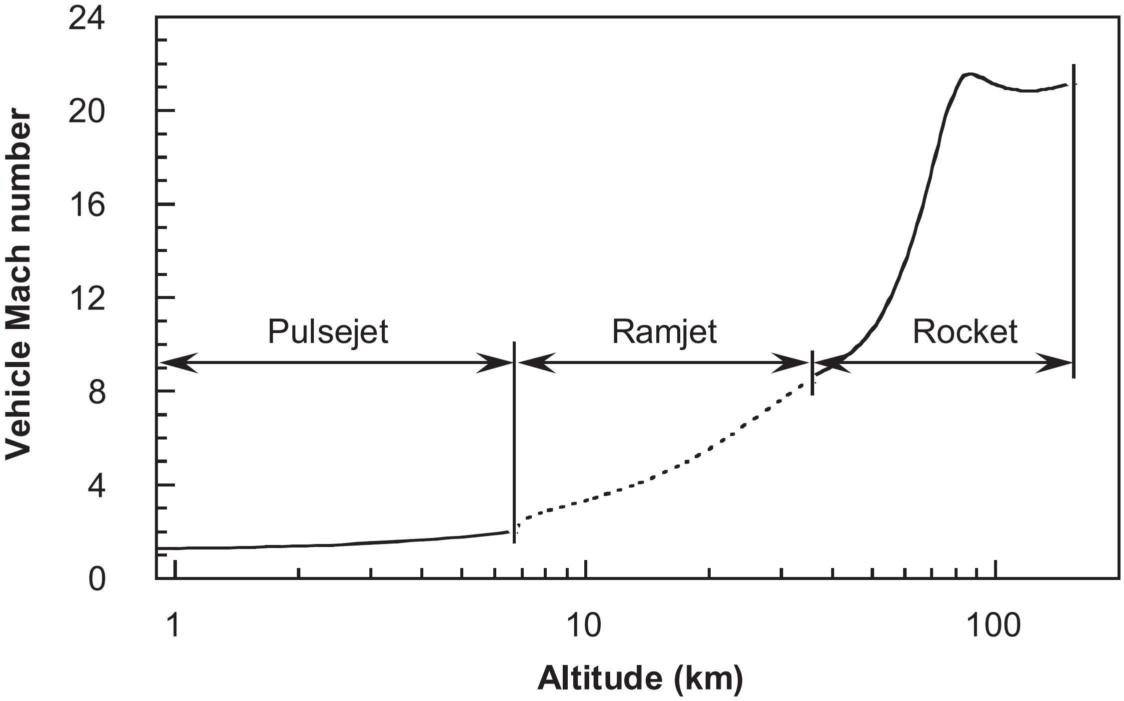

Figure 1.3: 100-kg-Vehicle trajectory through the three modes of laser propulsion in a vertical launch

1.4 Impulse generation process

The impulse generation processes for laser propulsion are divided into four processes as follow.

1. Breakdown of the gas and laser supported detonation (LSD) wave generation
2. Blast wave energy conversion
3. Impulse generation
4. Refill of the gas

This process is illustrated in Fig.1.4 A breakdown of the atmospheric air occurs by focusing an intense laser pulse. A plasma front propagates along the laser light channel while absorbing the laser energy. Then, the plasma drives a blast wave, and the blast wave energy is converted to the thrust work by a nozzle-shaped reflector [1][12]. Laser energy is absorbed and converted to the blast wave energy by the plasma in a laser supported detonation (LSD) regime [13]. The detail of the LSD wave is described next section.

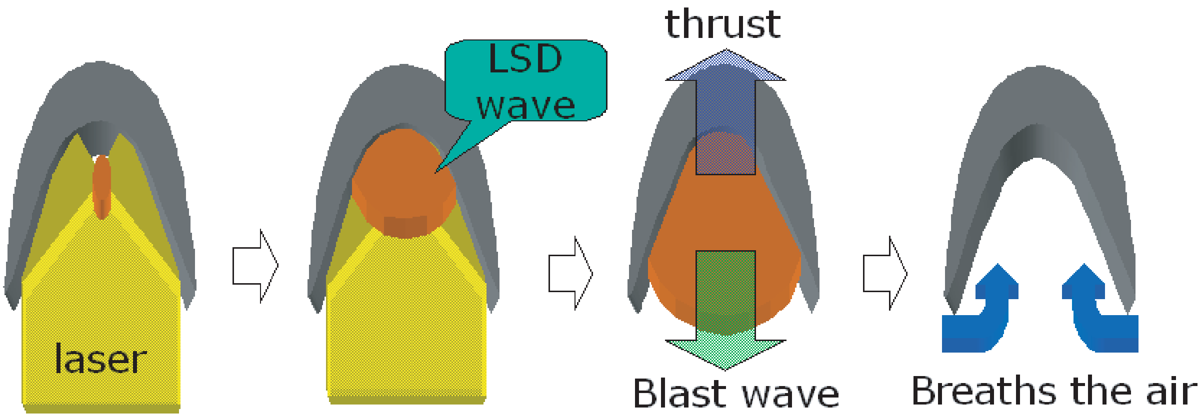

Figure 1.4: Impulse generation process

1.5 breakdown

Laser breakdown of the atmospheric air is initiated by focusing an intense laser pulse. The power density threshold for the breakdown was measured at he order of 10^3 to 10^4 MW/cm^2 using a CO2 laser. Laser breakdown process and laser-induced plasma generation process are as follows [12]. In the first stage, N2 and O2 molecules in the air are ionized by multi photon absorption. This phenomenon occurs when the simultaneous absorption energy of n photons, nhv, exceeds the ionization potential, where h stands for the plank constant and v stands for the frequency of the light. The minimum ionization energies of O2 and N2 are12.5eV and 15.8eV, so it could be estimated as n=11 for O2 and n=14 for N2 for a CO2 laser. The electron which generate in this first stage are called the first generation electron. In the second stage, the first generation electron is accelerated by the inverse-bremsstrahlung effect. These electrons remove other electrons from the order molecules and atoms. In this way, an electron avalanche develops. When the characteristic length of the ionization regime is parallel to the Debye length, a laser-induced plasma generates.

1.6 laser absorption process

After the laser induced-plasma is generated, the intense laser beam continues to be irradiated on the surface of this plasma. The laser energy is absorbed by this plasma mainly through the inverse-bremsstrahlung process. It is well known that the laser absorption mechanism is classified into two regimes. At laser power densities greater than the order of 10^7 W/cm^2, laser absorption occurs in Laser Supported Detonation (LSD) wave [14][15][16]. On the other hand, at power densities lower than 10^6/cm^2, it occurs in Laser Suppported Combustion (LSC) wave.

1.6.1 LSD regime

LSD wave travels at a supersonic velocity along the laser light channel in the direction opposite to the beam incidence. Although the mechanism of LSD wave propagation is not still clarified, existing an electron seed in the front of the strong laser absorption regime are considered to be essentially important. The electron seed is considered to be produced by mainly three effects.

1. shock compression effect
2. electron diffusion effect
3. photoionization or photoexcitation effect

The dominant effect in three effects is determined by the laser power density irradiated on LSD front.

Similarly to the chemical detonation wave, LSD wave is thought to have a Zel 'dovich-Nuemann-Doring (ZND) wave structure, in which cold gas ahead of the wave is compressed and heated in a shock front called the von-Neumann spike [17].

In general, very high temperature region radiate the ultraviolet-ray. The high energetic photon emitted from this region could directly remove or excite the electron of the molecules in the cold gas ahead of the thermal boundary layer. This is called photoionization and photoexcitation. The speed of the propagation of the discharge front is very high and in the hydrogen at 40Pa, the speed is estimated to be 10^6m/s [18]. Photoionization and photoexcitation is appeared in the radiation detonation phenomenon, for example, in the extraordinary explosion.

In LSD regime, very high energetic electrons, which are distributed in the foot of electron distribution function, are considered to exist. By the diffusion of the high energetic electrons, the laser absorption precursor is generated ahead of LSD front. This effect is reported to be essential to generate LSD wave in room temperature by Shiraishi [19].

The laser beam irradiated on LSD front could be reflected because the electron density in such a strong absorption regime would be near to the critical density for the incident laser beam. By principle of superposition, the reflected wave and the incident wave make the composite wave, which amplitude is twice as much as each one and which electromagnetic energy is four times as much as one. In this high electromagnetic energy, the cold gas ahead of LSD front occurs breakdown by multiphoton effect and this regime become new absorption regime.

1.6.2 LSD termination and LSC regime

The propagation of LSD regime terminates and transfers to LSC regime when the laser power density on the LSD wave front decreases to LSD threshold. In the LSC regime, laser absorption occurs in plasma mostly at uniform pressure. The absorption wave has a structure similar to a deflagration wave: it is called an LSC wave. The wave propagates in the direction opposite to beam incidence at a subsonic velocity due to heat conduction. After cold gas ahead of the wave is heated and ionized through heat condition, it expands to absorb the laser beam.

The propagation of LSD regime terminates when the laser power density on the LSD wave front decreases to LSD threshold. Since CO2 laser beam is absorbed mostly by the electrons through the inverse-bremsstrahlung process, and the fractional absorption of LSD wave, the shock wave interacts with the laser absorption region, and the irradiated energy is delivered efficiently to the motion of the surrounding air through the expansion work of the plasma after the LSD termination cannot generate a high presuure wave and has no contribution to the increment in the energy of the LSD termination may be converted into the radiation energy and the internal energy frozen in the plasma region. Larger duration of LSD existence in using the same laser system brings higher energy conversion efficiency from the laser pulse energy to the energy of the surrounding air motion.

Mori investigated systematically the LSD termination with different value of focusing f-number, laser energy and atmospheric pressure by using shadowgraph method [20]. Figure.1.5 shows the shadowgraphs of an exploding plasma and blast wave induced by a 10J-CO2 laser. Figure 1.6 shows the displacement of the shock front and plasma from the focus in the direction opposite to the laser incident channel. The coincident of each front occurs during LSD regime. After LSD regime termination, the shock front propagates further and the plasma front stays. The intersection point of the two curves indicates the timing of the transition from LSD regime to LSC regime.

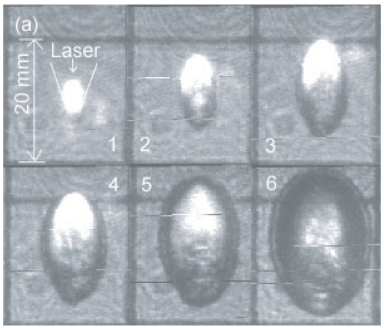

Figure 1.5: shadowgraph images for point focusing LSD wave

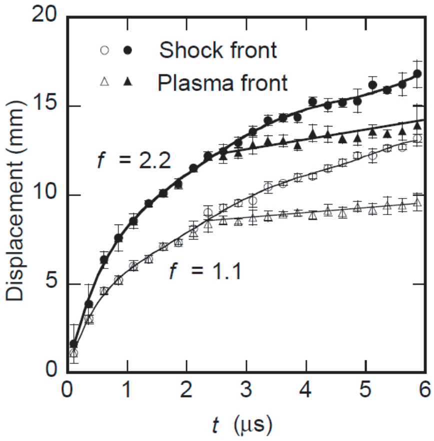

Figure 1.6: displavement of theshock front and plasma front for the point focusing LSD wave

1.7 Theory of LSD termination

As seen in the previous section, sustention of the LSD is effective in increasing the thrust performance of laser propulsion. Therefore, the theory of LSD termination by Raizer[?] is introduced in this section.

As seen in the Fig.1.7, heated and compressed gas in the zone where the LSD takes place expands not only along the direction of propagation of the shock wave, which causes the motion of this wave, but also in the lateral directions. This lateral expansion uses some of the energy which will not help the propagation of the detonation wave. The ratio of the energy lost as a result of this lateral expansion to the energy utilized in the propagation of the detonation is characterized by the ratio of the lateral surface $2\pi r \Delta s$ to the area of the wave front πr^2, i.e., it is characterized by the ratio $\Delta x/r$. Δx is the order of the path traveled by the incident radiation l. If the thickness l is of the order of or greater than r, the energy losses by the lateral expansion are so large that the input laser energy is insufficient to sustain the initiation shock wave. In practice, Raizer predicted that an LSD would terminate when $l/r \approx 4$.

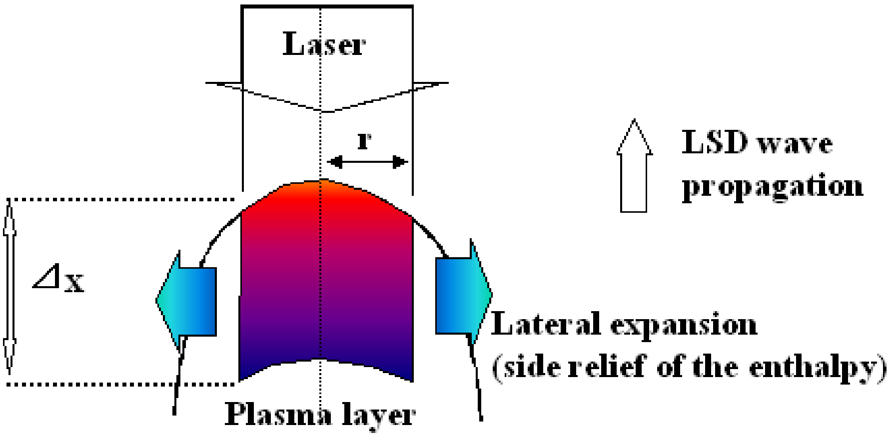

Figure 1.7: Schematic of a lateral expansion of an LSD.

In Raizer's theory, laser light channel geometry is one dimensional. However, in the laser propulsion, LSD is mainly generated in the cone shaped laser channel. In order to represent the ratio of energy lost by the lateral expansion to the energy utilized, a ratio

$$S_{side}/S_{front} \tag{1.1}$$

would be accurate in the case the geometry of the laser light channel differs. In this expression, Raizer's prediction of LSD termination would be as follows: LSD would terminate when $S_{side}/S_{front} \approx 8$. In this theory, LSD termination is determined only by the energy loss due to lateral expansion. This indicates the possibility of preventing the LSD termination by confining the lateral expansion.

1.8 Previous study

Usio et al investigated two and quasi-one dimensional LSD wave driven by a linearly focused laser beam using the shadowgraph method. The schematic of the shadowgraph experimental apparatus is shown in Fig.1.8. CO_2laser was linearly focused on an aluminum plate to initiate the breakdown in the atmospheric air. An off-axis linearly condensing parabolic mirror was used to focus the laser beam. Its focal length was 48mm. The 2D collector optics is shown in Fig.1.9(a). Besides, an aluminum wedge nozzle was used to realize quasi 1D LSD wave propagation by limiting the blast wave expansion in the direction perpendicular to the laser channel as Fig.1.9(b).

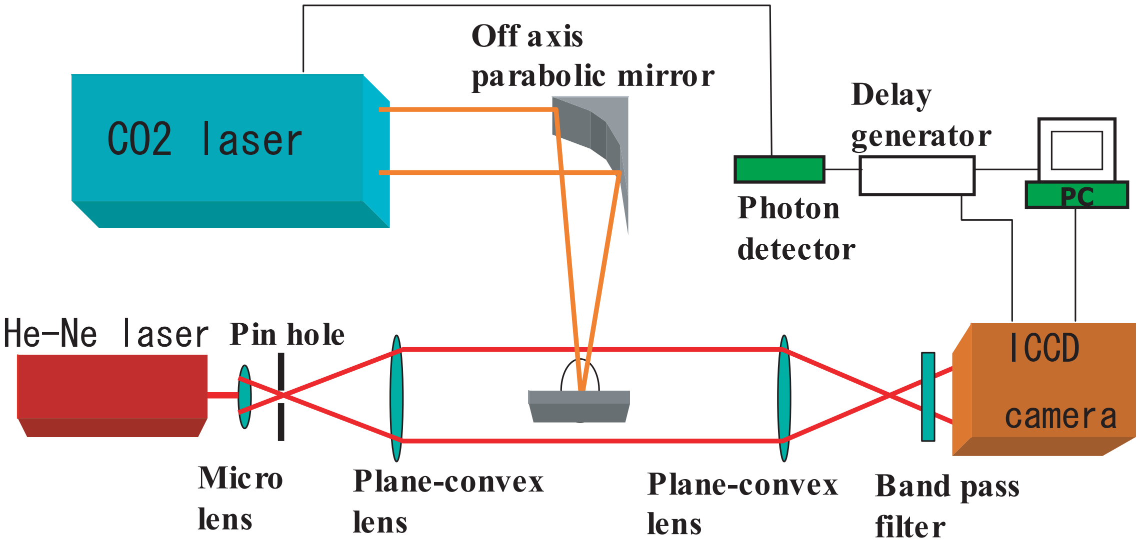

Figure 1.8: Schematic of the shadowgraph experimental apparatus

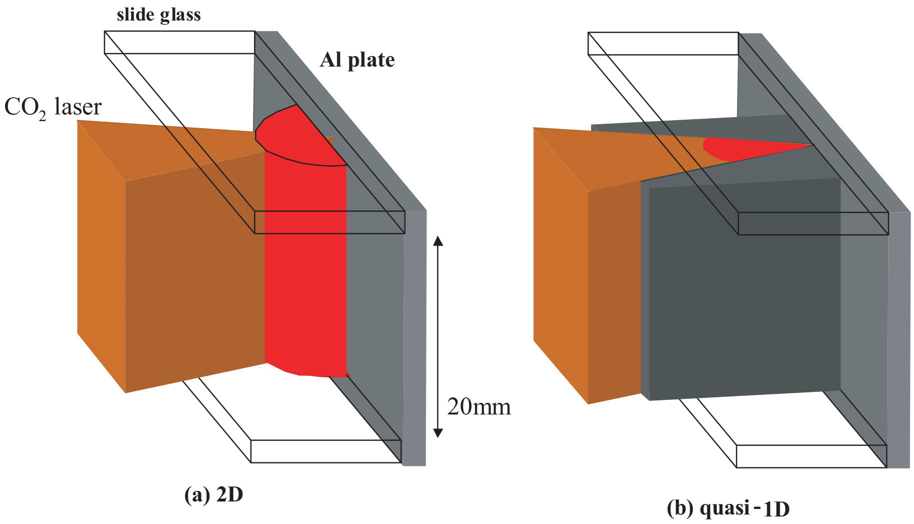

Figure 1.9: Schematic of 2D and quasi-1D collector optics

Fig.1.10 and Fig.1.11 shows theshadowgraph images of a 2D and quasi-1D LSD waves. Laser started to irradiate at t=0$micro$s. In these figures, a head of shadow is shock front and a head of emission is plasma front. Temporal variation of these fronts on the laser axis is shown in Fig.1.12 and Fig.1.13. As seen in the figures, the shock front and plasma front began to separate at 1.3$micro$s for the 2D LSD wave and 1.8$micro$s for the quasi-1D LSD wave.

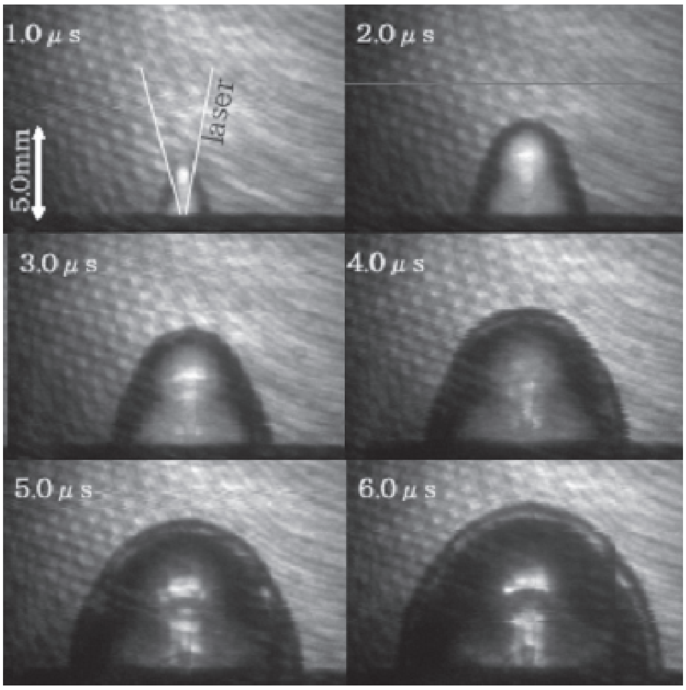

Figure 1.10: shadowgraph images of a 2D LSD wave

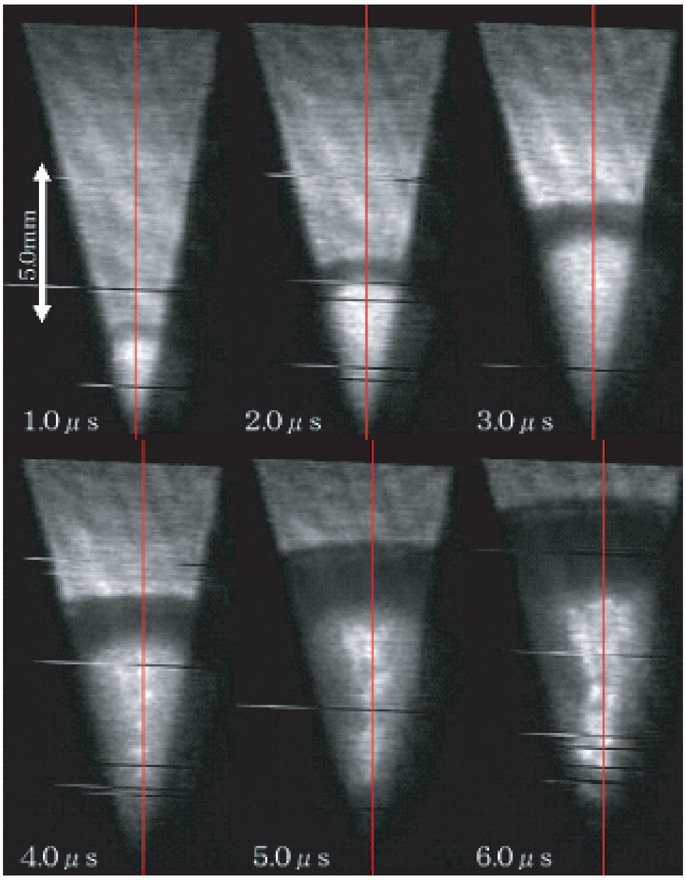

Figure 1.11: shadowgraph images of a quasi-1D LSD wave

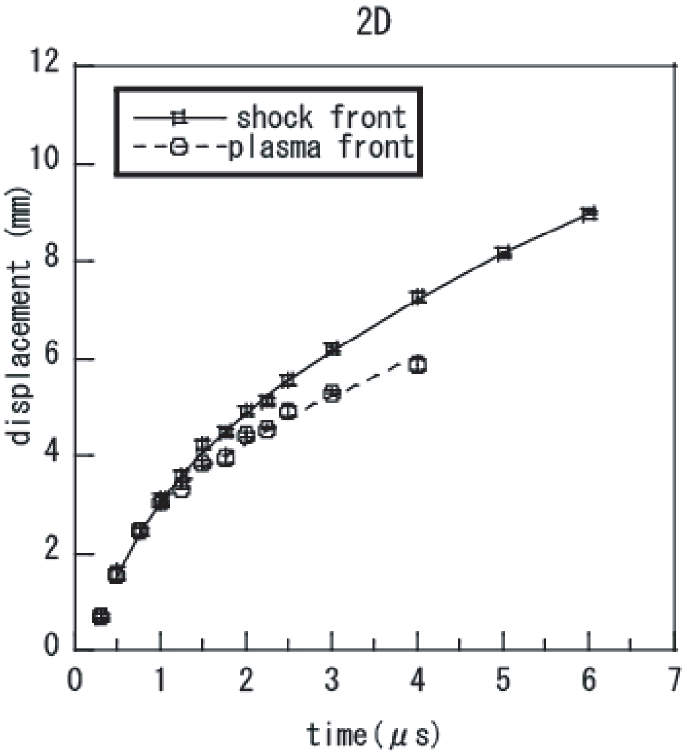

Figure 1.12: Displacement of the shock front and plasma front for the 2D LSD wave

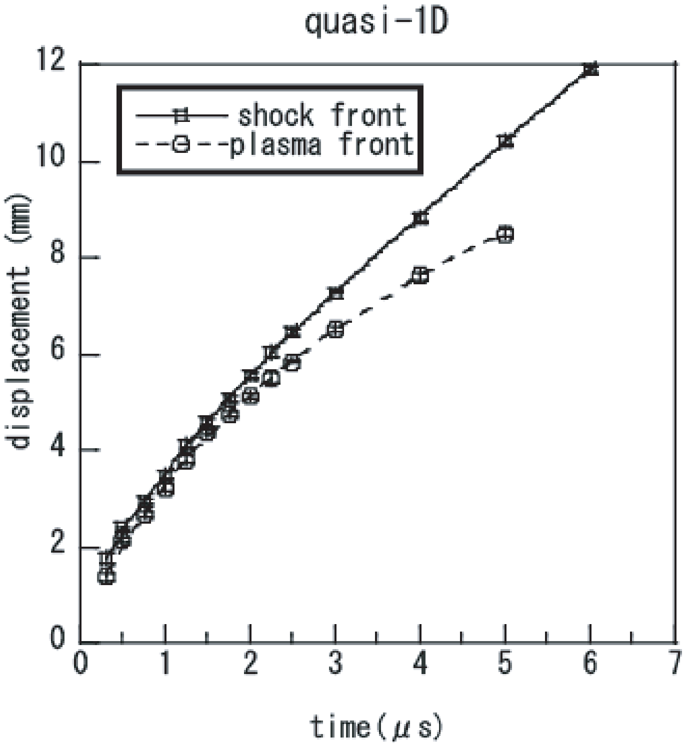

Figure 1.13: Displacement of the shock front and plasma front for the quasi-1D LSD wave

1.9 Objectives

The laser was line-focused on an aluminum plate, and generated line-focused LSD wave. Propagation direction was controlled and 2D and quasi-1D LSD waves was generated.

The electron number density distribution behind these LSD waves is measured by two-wavelength Mach Zehnder interferometry.

Furthermore some physical quantity is estimated in 2D LSD wave.

At the LSD termination, similarity of termination conditions between 2D and quasi-1D LSD wave is picked up.

From these results, one of the LSD termination condition is found out.

Chapter 2

Measuremnt of electron number density distribution

Our purpose is measurement the electron number density distribution behind the LSD wave. Two-wave length Mach Zednder interferometry that is was applied to measure the electron number density. Principle of Mach Zednder interferometry and the way to analyze theinterferogram is shown in this chapter.

2.1 Principle of Mach Zehnder Interferometry

In Mach Zehnder interferometry, coherency of light is used to determine the refractive index. This measurement method is one of the quantitative visualization methods. It has the advantage of noncontact method and enough to acquire the nonsteady phenomena.

The system of the Mach zehnder interferometry consists of two beam splitters and two plane mirrors as shown in Fig2.1. A homochromatic light from the light source is divided into two, and recombined on a screen. With slight difference in little path lengths, two lights interfere each other and make a interferometric fringe pattern. Where the difference in light path length is the same to $\lambda \times n$ (λ is wavelength, n stands for positive integer), they reinforce each other and become bright because two lights are in phase. On the other hand, where the difference is the same to $\lambda \times (n + 1/2)$, they cancel each other and become dark. When one of the lights propagates through the target object, difference of the refraction index in the object will be visualized quantitatively in the form of fringe pattern shift. (Thus one of the two lights is called a reference light and the other is called a probe light.) This fringe pattern shift is expressed as

$$h = \frac{1}{\lambda} \int \left(N_{ref}(z) - N_{flow}(z) \right) dz \tag{2.1}$$

where h is the number of fringe shift, z is the direction of the channel of the probe laser beam, N is the refractive index, λ is the wavelength of the light source. The subscripts "flow " and "ref" represent the case inside and outside(reference path) of the test section respectively. When the flow in the test section was homogeneous, with width of d, Eq.2.1 could be rewritten as

$$h = \frac{\left(N_{ref}(z) - N_{flow}(z) \right) d}{\lambda} = \frac{\Delta N d}{\lambda} \tag{2.2}$$

$$\Delta N = \frac{h\lambda}{d} \tag{2.3}$$

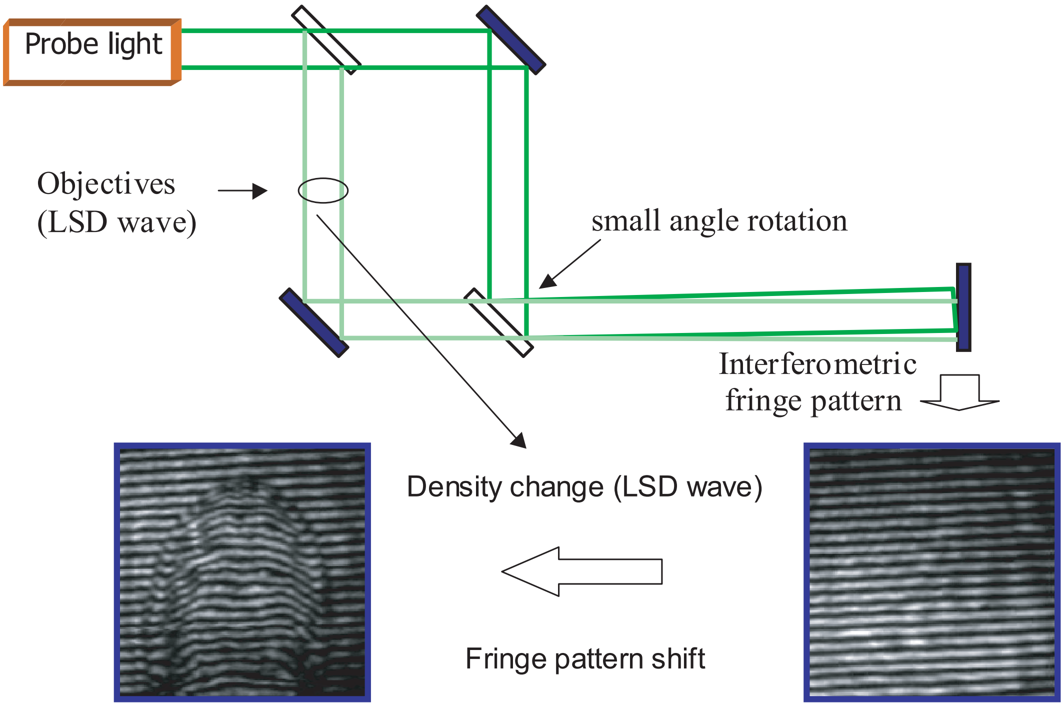

Figure 2.1: The fundamental system of Mach Zehnder interferometry.

where ΔN is the difference of the refractive index between the reference area and the object. Thus just by reading the shift of a fringe pattern, refractive index inside the target object will be known.

2.2 The relative refractive index of electron

A refractive index is defined as the ratio of the phase speed of the light in a given medium and in a vacuum. In this study, this medium corresponds to laser-induced plasma which consists of electrons, ions and neutral particles, and a blast wave which consists of neutral particles. In general, the refractive index N of the medium consisted of many species is approximately expressed as follows

$$N - 1 = \sum K_j n_j \tag{2.4}$$

where K_j and n_j are the relative refractive index and the number density of species j respectively. The medium in this study are consisted of three species; an electron, an ion, a neutral particle. The relative refractive indices of an ion and a neutral particle is approximately constant; K_i=7.4×10^{-}30 [m^3], K_n=1.1×10^{-}29[m^3]. On the other hand, the relative refractive index of electron is dependent on the wave length as seen in the Fig.2.2.[21] And its value is estimated from the dispersion relation of the electromagnetic wave propagating in plasma under the assumption of no magnetic field. The dispersion relation is as follows,

$$\omega^2 = \omega_{pe}^2 + k^2 c^2 \tag{2.5}$$

$$\omega_{pe} = \sqrt{\frac{n_e e^2}{m_e \varepsilon_0}} \tag{2.6}$$

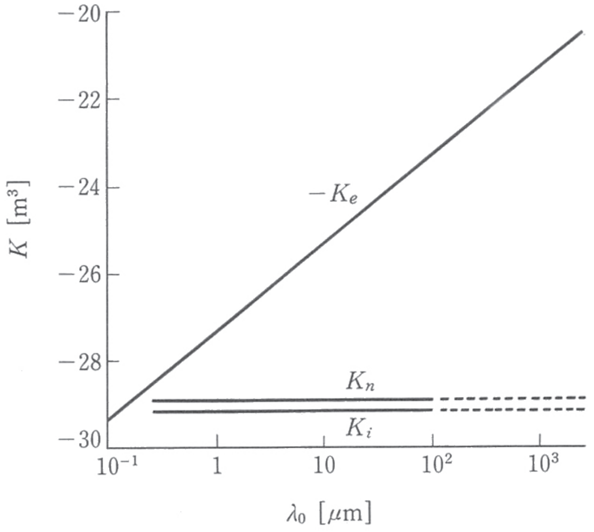

Figure 2.2: The dependence of the refractive indices on the wave length.

where ω, k is the angular frequency and the wave number of the electromagnetic wave in a plasma, respectively, and ω_{pe} is the plasma frequency. c, ε are the light velocity and the permittivity of free space, and n_e, m_e, e are the electron number density of the plasma, the electron mass and electron charge, respectively. The refractive index of an electron to the electromagnetic wave of angular frequency ω, is

$$N_e = kc/\omega \tag{2.7}$$

Using Eqs.2.5 and2.7, the following equation are derived.

$$N_e = \left(1 - \left(\frac{\omega_{pe}}{\omega}\right)^2\right)^{1/2} \tag{2.8}$$

Under the additional assumption, Eq.2.5 is

$$N_e - 1 = -\frac{\omega_{pe}}{2\omega^2} \tag{2.9}$$

From Eq.2.4, the relative refractive index is expressed as follows

$$K_e = -\frac{e^2}{8\pi^2 c^2 m_e \varepsilon_0}\lambda^2 \tag{2.10}$$

where λ is the wavelength of the electromagnetic wave. As seen in Eq.2.10, -K_e is proportional to the square of the wavelength.

K_i and K_n is approximately constants. In contrast, K_e is dependence on the wavelength of probe laser. In the two-wavelength Mach Zehender interferometry, this dependence is used to measure the electron number density. The detail was described next section.

2.3 Reflactive-index change

Using Eq.(2.3) and (2.4),

$$\Delta N = \frac{h\lambda}{d} = \sum_{ref} K_j n_j - \sum_{flow} K_j n_j \tag{2.11}$$

$$= K_n n_0 - (K_n n_n + K_i n_i + K_e n_e) \tag{2.12}$$

where K is a relative refractive index and n is a number density. The subscripts, n, i, e, represent a neutral particle, an ion, an electron, respectively. n_0 is the number density of the neutral particle in the atmospheric air (reference path was set in the atmospheric air).

Without any assumption, contribution of the number density of each particle to the total refractive index cannot be identified from simple Mach Zehnder interferometry and this equation. However, by using the dependency of K_e to the wavelength as above, contribution of the electron density would be extracted. The detail of this method is described in the next section.

2.4 Two-wavelength Mach Zehnder interferometry

The large dependence of the electron component and the relatively small dependence of the other plasma constituents on the probe light wavelength make it possible to determine electron density, even in the presence of contributions to the refractivity from the nonelectronic constituents. This is accomplished by simultaneous measurement of the refractive index of the plasma at two wavelength.[22] By two-wavelength Mach Zehnder interferometry using the wavelength λ_1 and λ_2, ΔN_1 and ΔN_2 would be known from Eq.2.12 and 2.10 as follows,

$$\Delta N_1 = K_n n_0 - (K_n n_n + K_i n_i + K_{e1} n_e) \tag{2.13}$$

$$= K_n n_0 - K_n n_n - K_i n_i - \left(-\frac{e^2}{8\pi^2 c^2 m_e \varepsilon_0}\lambda_1^2\right) n_e \tag{2.14}$$

$$\Delta N_2 = K_n n_0 - (K_n n_n + K_i n_i + K_{e2} n_e) \tag{2.15}$$

$$= K_n n_0 - K_n n_n - K_i n_i - \left(-\frac{e^2}{8\pi^2 c^2 m_e \varepsilon_0}\lambda_2^2\right) n_e \tag{2.16}$$

where K_1 and K_2 is the relative refractive index of the electron for each wavelength. By substituting Eq.2.16 from 2.14, n_e is expressed as follows.

$$\Delta N_1 - \Delta N_2 = \frac{e^2}{8\pi^2 c^2 m_e \varepsilon_0}(\lambda_1^2 - \lambda_2^2) n_e \tag{2.17}$$

n_e is expressed from Eq.(2.17) as follow

$$n_e = \frac{1}{(\lambda_1^2 - \lambda_2^2)}\left(\frac{8\pi^2 c^2 m_e \varepsilon_0}{e^2}\right)(\Delta N_1 - \Delta N_2) \tag{2.18}$$

As Eq.(2.18), using couple of ΔN, the electron number density is calculated.

In addition, under the assumption of the singly ionized plasma n_e=n_i, the nutral particle number density is derived from Eqs.2.14 and 2.18.

$$n_n = n_0 - \frac{\Delta N_{1or2} - (K_i + K_{e1or2}) n_e}{K_n} \tag{2.19}$$

Chapter 3

Experimental Apparatus

In this chapter, the system of apparatus as follow was used to measure the electron number density distribution

- 1) For generating line-focused 2D and quasi-1D LSD wave
- 2) Two-wavelength Mach Zehnder interferometer

These details of the system was shown.

3.1 Apparatus for Generating LSD

In this study, linearly focusing LSD wave was generated. A 10 J Transversely Excited Atmospheric (TEA) CO_2 pulse laser was used to generate the linearly focusing LSD wave, as Fig.3.1. The laser was line-focused on an aluminum plate to initiate the breakdown in the atmospheric air. An off-axis line-focusing parabolic mirror was used to focus the laser beam. Details of these apparatus and the whole system to generate the LSD are shown in this section.

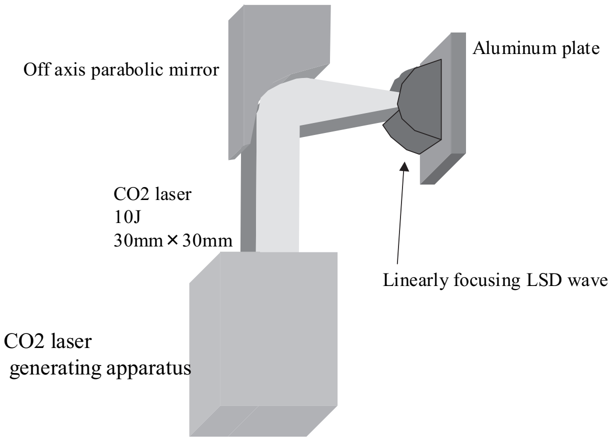

Figure 3.1: schematics of the LSD generating apparatus

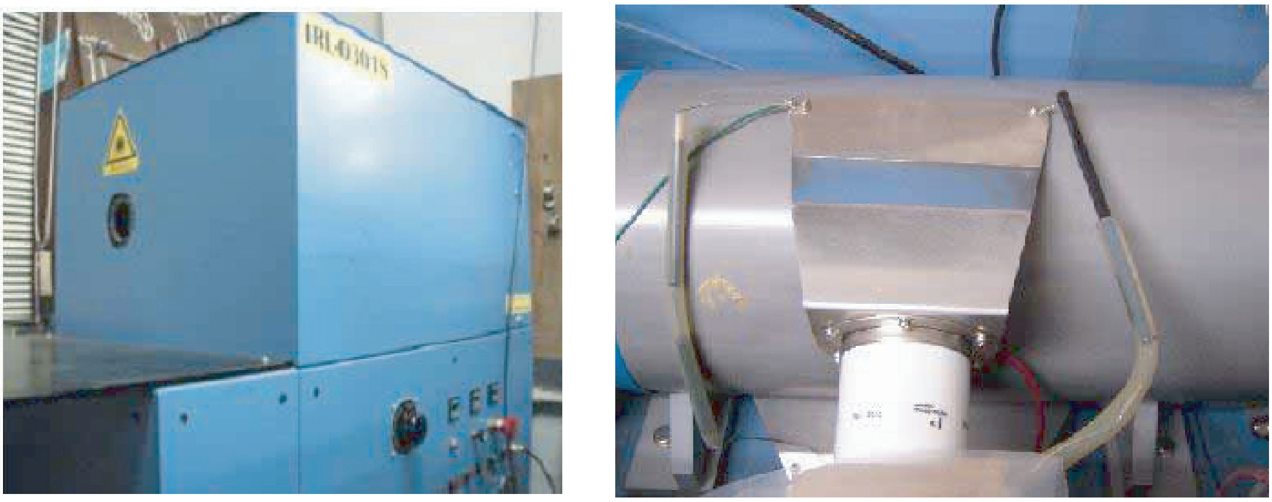
(a)

(b)

Figure 3.2: Picture of TEA CO_2 pulse laser. (a) Exterior of IRL-1201, (b) laser-dixcharge tube and gap-switch.

3.1.1 TEA CO_2 pulse laser

Plasma was produced by Transversely Excited Atmospheric (TEA) CO_2 pulse laser whose nominal energy E_i was 10 J. The laser was made by Usho optical system co. ltd. Its specification is summarized in Table 3.1. Its exterior is shown in Fig.3.2(a). Laser excitation is initiated by triggering the discharge in the gap-switch shown in Fig.3.2(b). The electric circuit is shown schematically in Fig.3.3. Voltage applied to the capacitor is controlled using a slide-regulator, and E_i can be changed slightly using the slide-regulator. E_i also depends on the fill-pressure in the laser-discharge tube. Figure 3.4 shows the relation between E_i and the fill-pressure. E_i increases with the fill-pressure. Pulse energy was measured before and after experiments using a joule-meter; consequent shot-to-shot pulse-energy fluctuations were maintained below 5% throughout experiment.

Table 3.1: The specification of TEA CO_2 laser.

Product No.	IRL-1201
Max. E_i	10 J
Repetition	single, $0.1\sim0.5$ Hz
Gas fill pressure	110kPa,a
Impressed voltage	~10kV
E_i fluctuation	$> \pm 5\%$
Power source	AC 100V 50/60Hz
Laser gas composition	$He:N_2:CO_2 = 84:8:8$

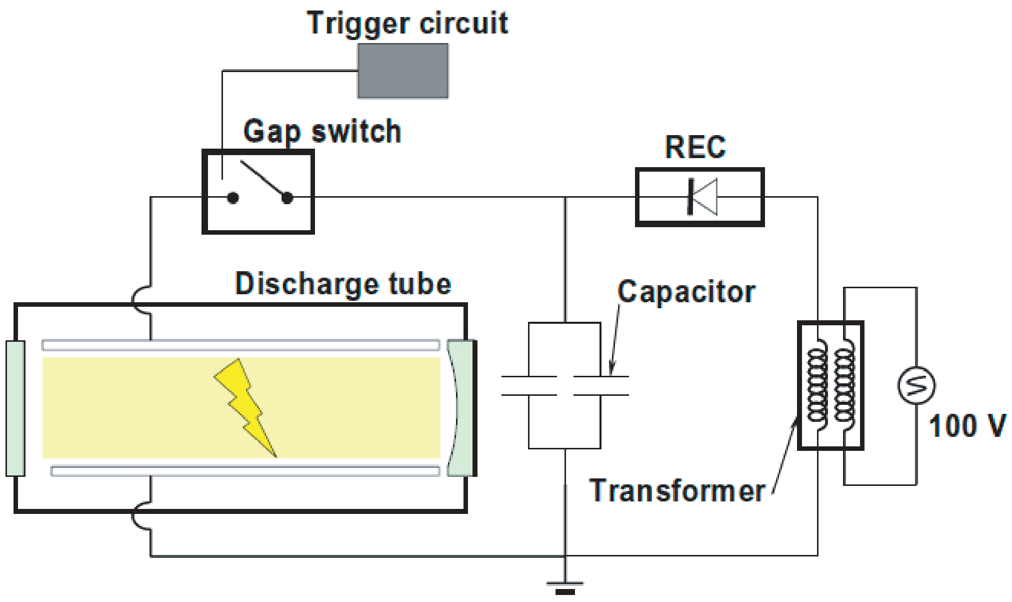

Figure 3.3: Electrical circuit for the TEA CO_2 laser.

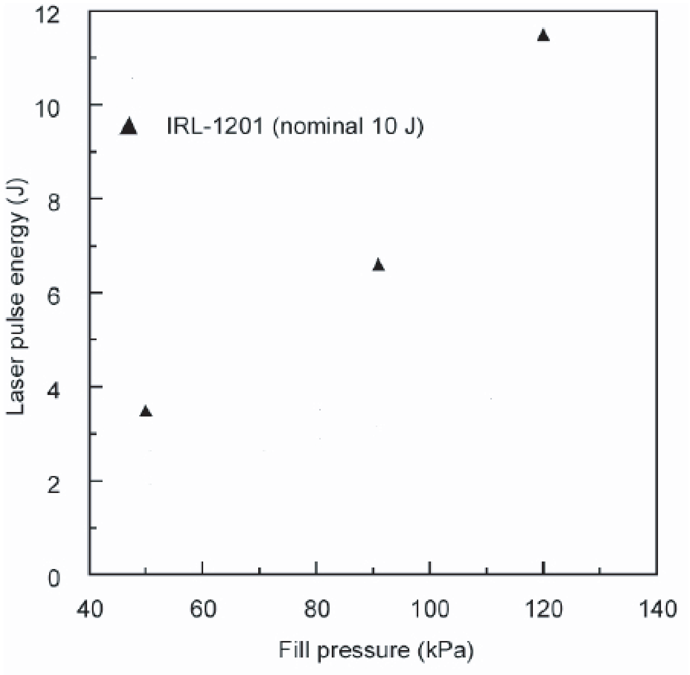

Figure 3.4: Relation between the laser pulse energy and the fill-pressure in the laser-discharge tube.

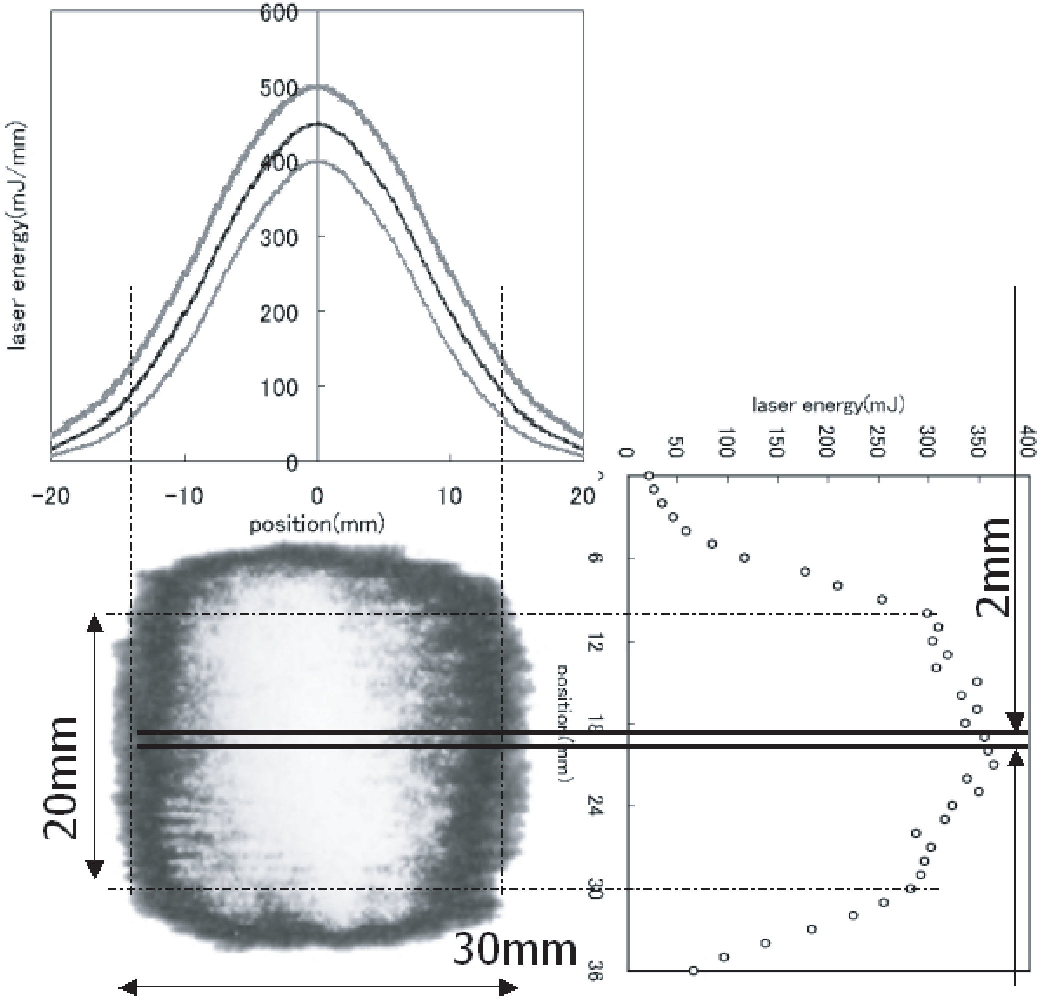

Figure 3.5: Energy distribution of the laser beam.

The laser beam was in the high-order multi-transverse mode: its beam quality factor was approximately 18. Energy distribution of the laser beam was measured using a joule-meter as shown in Fig.3.5. The burn pattern of the laser beam is also shown in the figure. It has gaussian distribution on the horizontal axis, and trapezoidal distribution on the vertical axis. The laser beam cross-section can be approximated by a 30 ×30 mm square. Equivalent beam diameter was 34 mm, which was the diameter of a circular beam having the same cross sectional area as the square beam. As in the figure, 20mm height area was used to generate the line focused LSD and that with confinement, while 2mm at the center was used to generate the thin LSD for interferometry.

Pulse shape was measured using a photon-drag detector (Hamamatsu photonics-B749) shown in Fig.3.6. The specification of the detector is summarized in Table 3.2. Typical pulse shape is shown in Fig.3.7. A leading-edge spike appears and an exponentially decaying tail follows. The shape is typical for TEA CO_2 pulse lasers. FWHM of the spike was 0.12 ± 0.02 μ s. The temporal change in the power at the tail $P_{tail}(t)$ can be approximated as

$$P_{tail}\{t\} = P_{0,tail}\exp\left(-\frac{t}{\tau_d}\right) \tag{3.1}$$

The pulse shape is influenced by the fill pressure in the discharge tube. Figure 3.8 shows the relation between the laser pulse shape and the fill-pressure in the laser discharge tube. The decay-constant of the tail τ_d decreases with the fill-pressure. The duration of the laser irradiation is mostly proportional to the duration of the excitation discharge, which is presumed to decrease with the fill-pressure of the gas in the tube. At the fill-pressure lower than 50 kPa, the reproducibility of the laser pulse shape became quite poor due to the instability of the excitation discharge in the tube. Tests were performed at the fill-pressure lower than 120 kPa for the safety of the discharge tube. With the nominal fill pressure at 110 kPa, the tail decay-constant τ_d was 1.15 ± 0.05 μs. The fraction of E_i that is contained in the tail was approximately 75 %.

Table 3.2: The specification of Photon-drag detector(Hamamatsu photonics, B749).

Aperture diameter	5mm
Sensitivity	1.2 V/MW
Rise time (10∼90%)	$<$ 1 ns

Figure 3.6: Photon-drag detector.

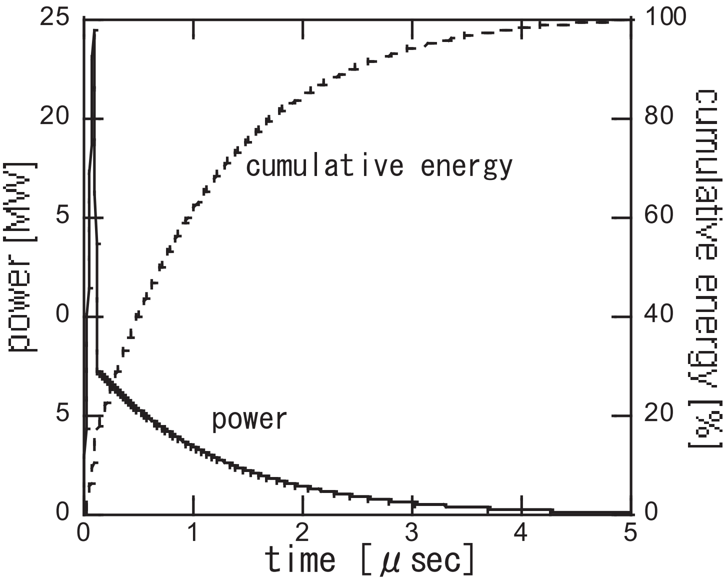

Figure 3.7: Laser pulse shape typical for IRL-1201.

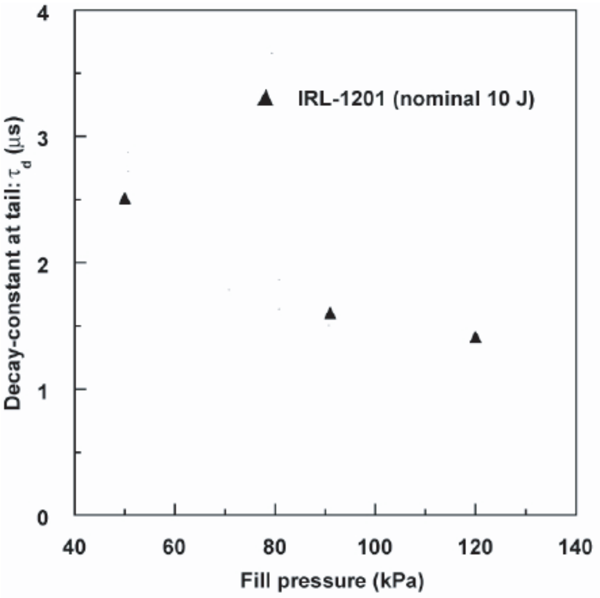

Figure 3.8: Relation between the decay-constant at the exponentially-decaying tail and the fill-pressure in the laser-discharge tube.

3.1.2 An off-axis line-focusing parabolic mirror

The laser beam was focused using an off-axis line-focusing parabolic mirror that was free from aberration. The schematic of the mirror is shown in Fig.3.9. Its focal lengths was 48 mm along the optical axis; its corresponding focusing f-number was 1.5. (Here, "corresponding f-number" is defined as laser focal length / laser beam width.) It reflects an incident laser beam by 90 degrees along the optical axis into focus. Line width on the focus was estimated at 0.25 mm.

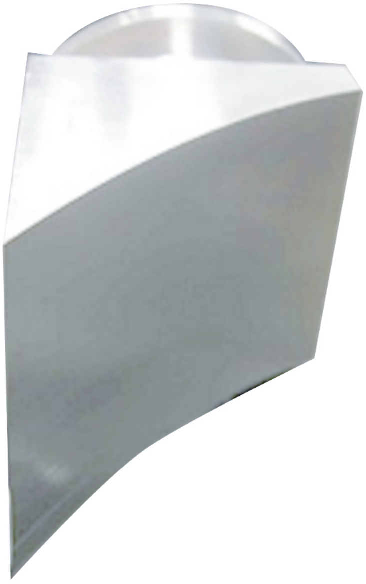

Figure 3.9: The schematic of the off-axis line-focusing parabolic mirror.

3.1.3 Collector optics

As seen in Fig.3.10, the laser was line focusing on an aluminum plate to initiate the breakdown in the atmospheric air. In this experimental condition, ablation of the aluminum was necessary to generate the LSD wave. Two glass walls were attached perpendicularly to the aluminum plate to prevent LSD wave spreading up and down. In this study, the LSD was generated in 2mm height space in order to modify the strong refractive effect. Then laser intensity on the shock front is exactly similar to shadowgraph experiment that is shown in section 1-8. Therefore motion of LSD wave 2mm thick is much the same to 20mm case. This detail is described later section.

As seen Fig.3.10(b) and Fig.3.11 an aluminum wedge nozzle was used to realize quasi-1D LSD wave propagation by preventing expansion in the direction perpendicular to the laser channel. This nozzle shape is similar to the converging angle of CO_2 laser light. As seen Fig.3.10(b) and Fig.3.11 an aluminum wedge nozzle was used to realize quasi-1D LSD wave propagation by preventing expansion in the direction perpendicular to the laser channel. In Fig.3.11, the region of space around nozzle were necessary to ambient fringe pattern to measure the density distribution as Fig.3.12. Because the information of the fringe pattern on the center before LSD wave propagation was interporated ambient fringe pattern. This detail was described in the Capter 4-2-2.

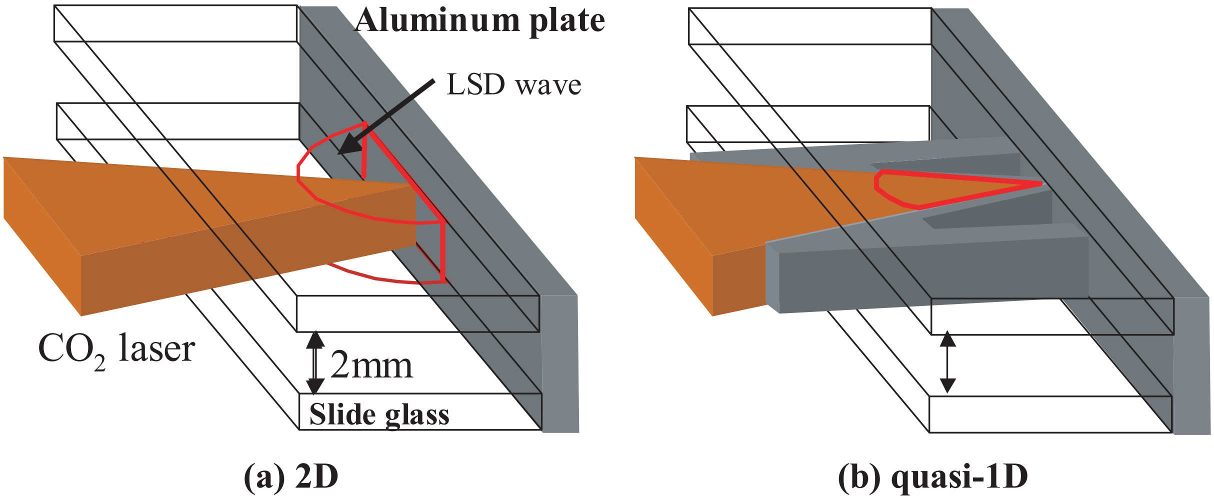

Figure 3.10: The schematic for propagation of the LSD wave.

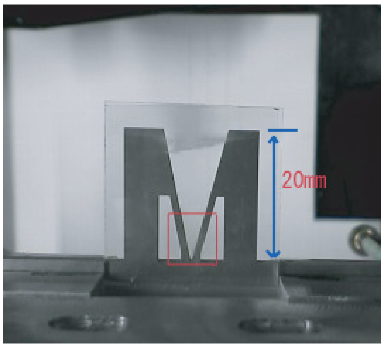

Figure 3.11: Nozzle shape.

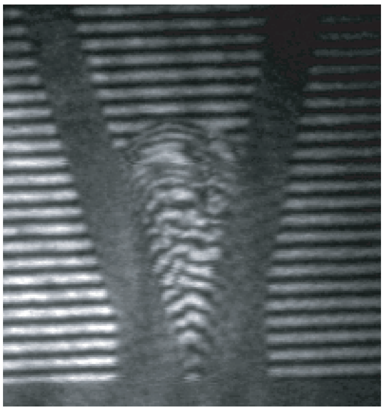

Figure 3.12: The image of the firinge pattern in quasi-1D case.

3.1.4 ICCD camera

The shadowgraphs and Mach Zehnder interferograms were taken using an ICCD camera (Oriel Instruments InstaSpecV^{TM} ICCD detector, Model 77193-5) shown in Fig.3.13. It's dependence of the quantum efficiency on the wavelength is shown in Fig.3.14. The camera image intensifier was operated as a shutter and an optical emission from the gap-switch of the laser discharge tube was used to trigger the shutter: strong emission from the gap-switch prior to laser oscillation was detected by a photo-sensor through an optical fiber. The measurement sequence is shown in Fig. 3.15. Soon after the gap-switch was triggered, its emission was initiated to trigger the measurement system. The laser irradiation started about 200 ns after the gap-switch ignition. The photo-sensor signal was transmitted to a delay-circuit (Stanford Research Systems, Inc., Digital Delay/Pulse Generator Model DG535), which allowed the setting of a delay period from the beginning of the laser pulse. The whole imaging set-up is shown with the shodowgraph system in Fig.3.16.

Figure 3.13: InstaSpecV^{TM} ICCD detector.

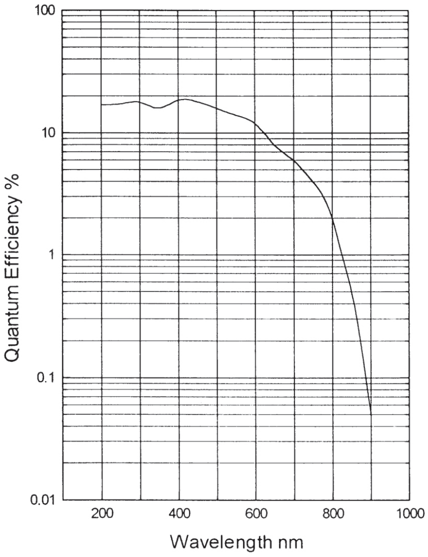

Figure 3.14: Typical quantum efficiency versus wavelength.

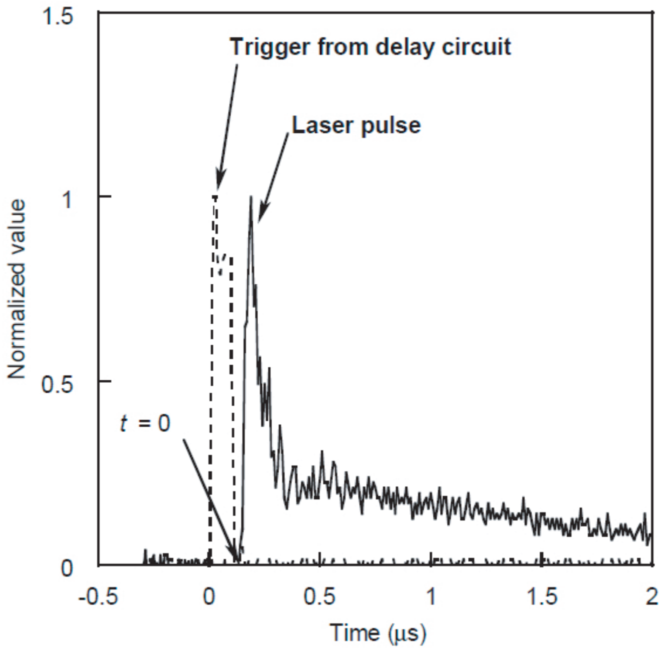

Figure 3.15: Measurement sequence: the laser pulse was measured using a photon-drag detector.

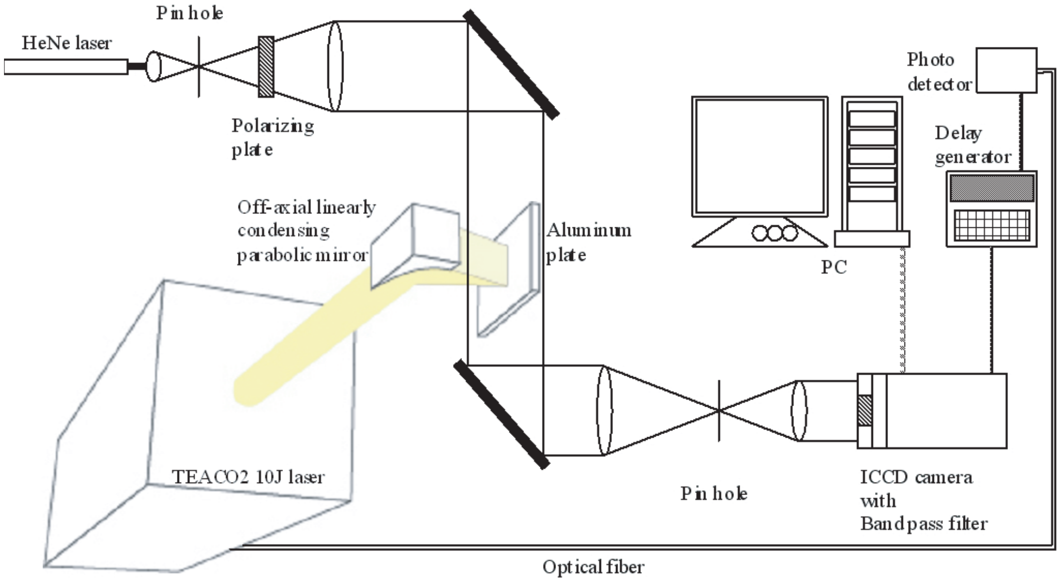

Figure 3.16: Imaging setup.

3.2 Interferometer

3.2.1 Two-wavelength Mach Zehnder interferometer

The system of two wavelengths Mach Zehnder interferometer is shown in Fig.3.17. The list of the optical equipments in this system is shown in Table.3.3. The detail of this system was shown Fig.3.18,3.19 and 3.20. The Pin-hole.2 and band pass filter at 532nm and 633nm are used to remove the strong emission by plasma. In the table, width and height of the Pin-hole.2 is different. This is due to the following effect. When the pinhole diameter was small enough (< 10 mm), diffractive effect becomes indispensable. The probe laser diffracts prominently, especially when the phase of the probe laser was perturbed in the phenomena. On the contrary when the pinhole diameter is large (> 4mm), plasma emission cannot be removed. Therefore, pinhole width was set in order tiremove the plasma emission sacrificing the clear interferogram in this direction, and height was to visualize the phenomena without the distribution of the diffractive effect in the direction of the target density distribution.

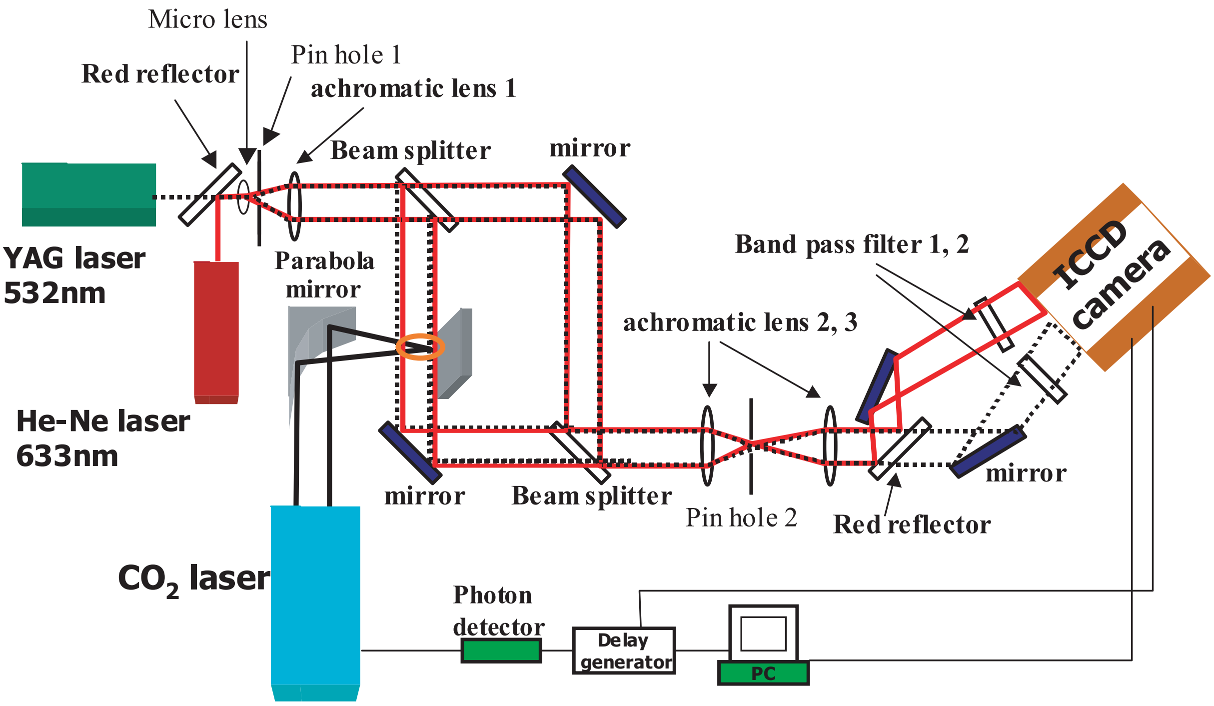

Figure 3.17: Two-wavelength Mach Zehnder interferometer

Table 3.3: Specifications of optical equipments.

	specifications
Pin-hole.1	ϕ=10[μm], 50MW/cm^2
Pin-hole.2	3mm width, 12mm hight
Micro lens.1	f=15[mm]
Achromatic lens.1	f=250[mm]
Achromatic lens.2	f=500 $\sim$ 800[mm]
Achromatic lens.3	f=500 $\sim$ 800[mm]
Red reflector	green:transmission red:reflection (Thorlabs)
Beam splitter	1:1
Band-path filter.1	λ=633±1nm
Band-path filter.2	λ=532±1nm

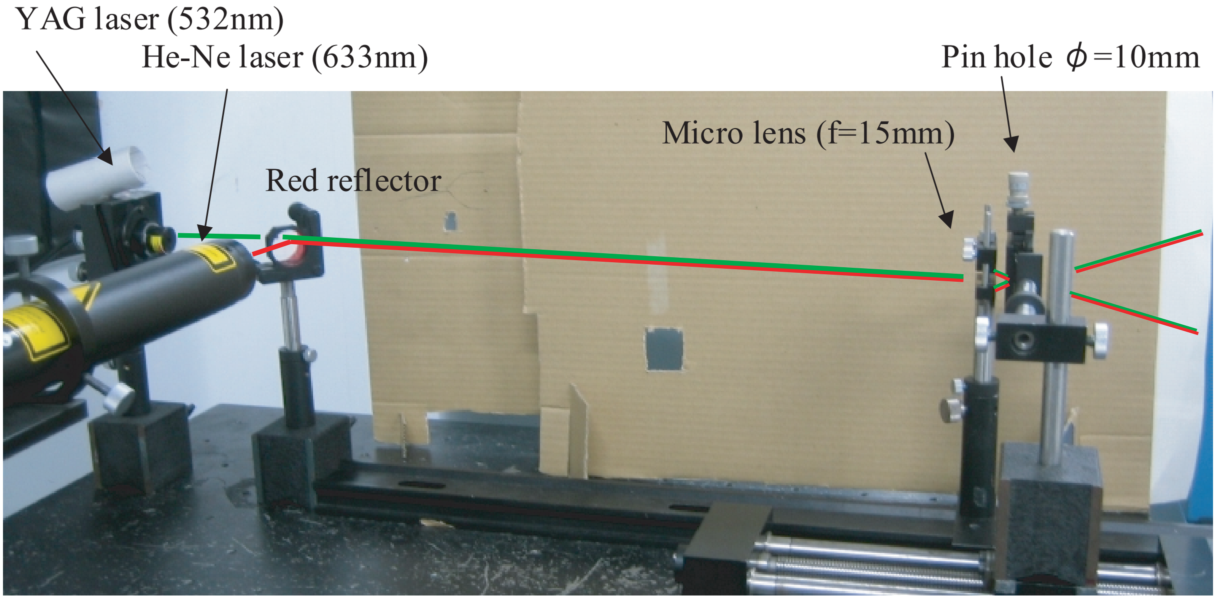

Figure 3.18: Shematics Two-wavelength Mach Zehnder interferometer (a)

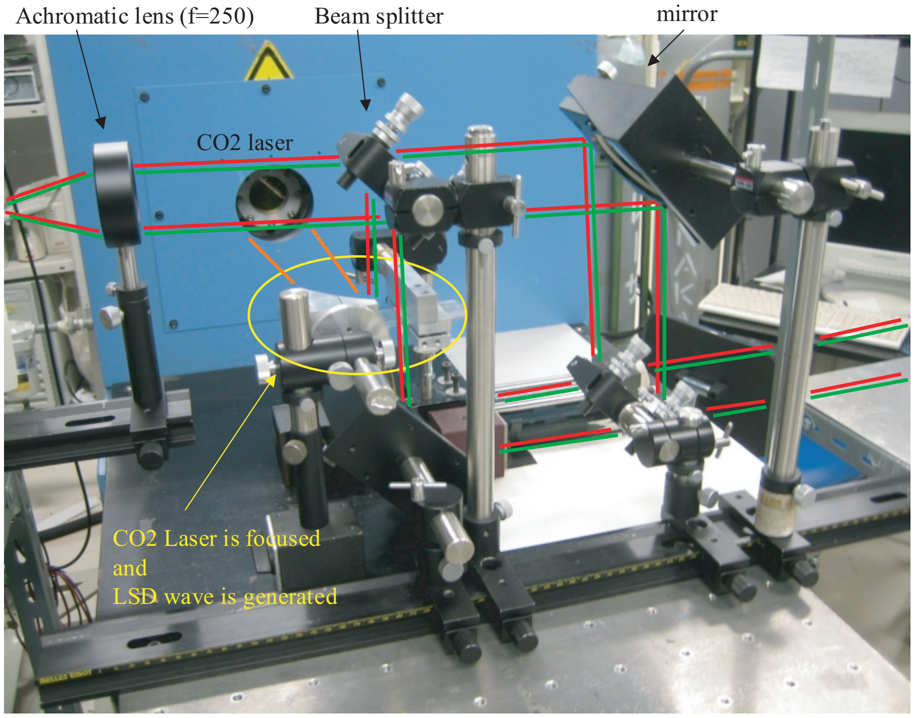

Figure 3.19: Shematics Two-wavelength Mach Zehnder interferometer (b)

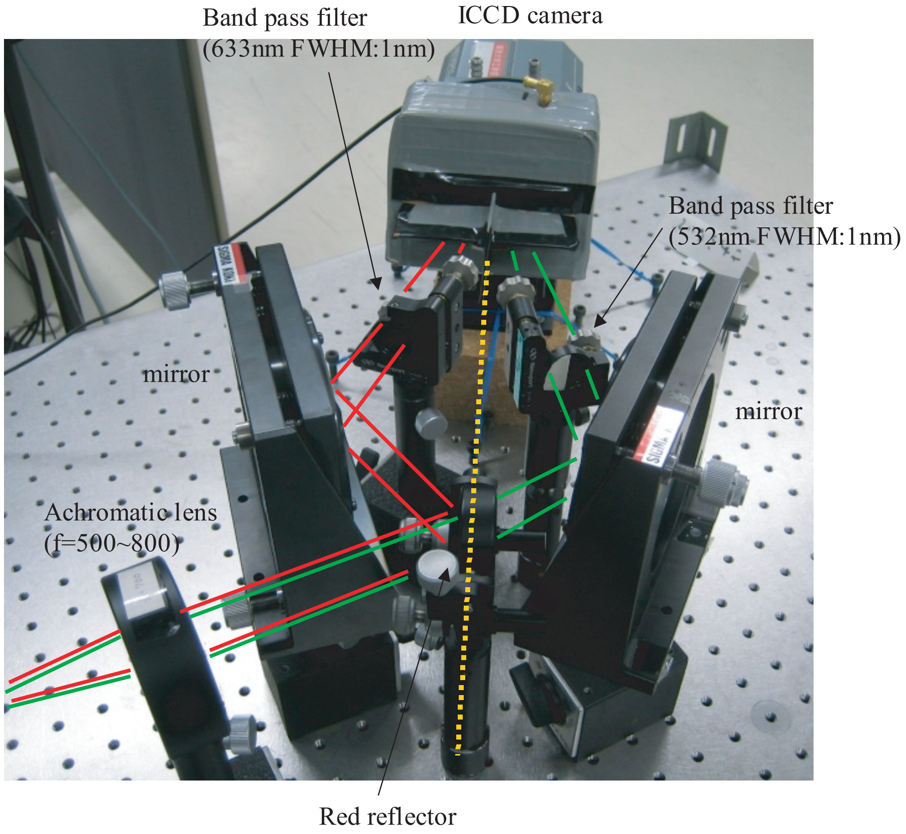

Figure 3.20: Shematics Two-wavelength Mach Zehnder interferometer (c)

3.2.2 Probe Laser source and Red reflector

A He-Ne laser and a diode pumped green laser were used as a light source of visualization. These lasers were combined using a red-reflector (Thorlabs, Inc.), which transmits the 532nm(green) light while reflecting the 633nm(red) light. Its dependence property of the reflectance ratio on the wavelength is shown in Fig.3.21. Combined laser was focused to the pinhole by the objective lens, and dirty spatial profile was collimated to be clean. (This apparatus is called spatial filter.) Clean profiled light from spatial filter, was parallelized by another lens. As a laser was used for the light source, its high coherency produced a obstructive fringe pattern (which was like a Newton ring), by the interference of the transmitted laser light and the reflected laser light of the objective lens.

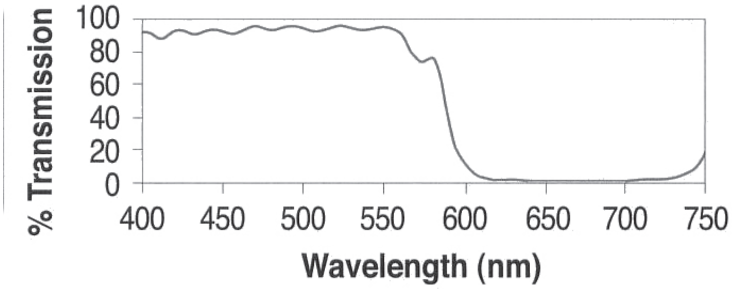

Figure 3.21: Red-reflector's dependence property of the reflectance ratio on the wavelength.

3.2.3 Achromatic lens

Using conventional optical lens, slight difference of the f-number between irradiated laser wavelengths, which is called chroma aberration, is occurred. Table.3.4 shows difference of the f-number with laser wavelength. This difference is cause of a faint image and difference of diameters two (633nm and 532nm) images. It is important for digitalization of fringe pattern to display crisp images. Using the achromatic lens, optical system with very little chromatic aberration is set and clearer images was produced.

Table 3.4: chromatic aberration of conventional plane-convex lens

f-number	wavelength-1 (515nm)	wavelength-2 (590nm)	wavelength-3 (633nm)
250mm	249.5	251.0	251.9
500mm	499.0	501.9	503.9
700mm	698.7	702.7	705.4

Chapter 4

Result and Discussion

The fringe pattern images in LSD wave were taken with Two-wavelength Mach Zehnder interferometer. The electron number density was conduced these fringe pattern shift. In this chapter, the result was divided into three parts as follow 1) interferograms, 2) method of conversion from these images to electron number density, 3) electron number density distribution. Then the discussion of these results was described.

4.1 Two-wavelength interferograms

Fig.4.1 shows two-wavelength interferograms of 2D propagation LSD wave for 532nm (left side) and 633nm (right side). In otherwise,4.2 shows interferograms of quasi-1D LSD wave. In these figures, laser started to irradiate at t=0$micro$s. In irradiate the pulse CO_2 laser, one time one image is taken. In the image, two wavelength (532nm and 633nm) interferograms are taken.

4.2 Method of conversion from interferograms to electron number density

In this analysis, the electron number density distribution on the center axis of the LSD wave was contributed. This analysis is spirited into three parts as

1) Digitalization and graph visualization of contrasting of the interference fringes.
2) Derivation of refractive-index change from displacement of the fringes.
3) Calculation of a jump of the fringe pattern on the shock front. (Only 2D LSD wave)

4.2.1 Digitalization

The variance of the brightness and darkness on the center axis was extracted from the visualized data of LSD, as Fig.4.3. Local shift of the fringe pattern was digitalized by detecting the peaks of contrast in this data as seen in figure.

4.2.2 Derivation of refractive-index change

Fig.4.4 shows number of fringe shift in the LSD wave. In this figure, fringe pattern on center axis before the LSD wave was interpolated from ambient and untinged from LSD wave fringe pattern, as Fig.4.5. Using eq.(2.14),(2.16), refractive-index change is calculated each wavelength (532nm and 633nm) as Fig4.6.

However, on the shock front, the jump of fringe pattern is occurred. Therefore movement distance is added this influence. As the Fig.4.4, the density increases repidly on the shock front and fringe shift is rapidly. Therefore, fringe shift is discontinuity and added *alpha* behind the shock front. To know about value of jump is so difficult to cut of the information of fringe. If this jump isn 't known, shape of the electron number density distribution is derived, but the position of zero point of the electron number density profile isn 't known. The method of calculation of this jump is shown next section.

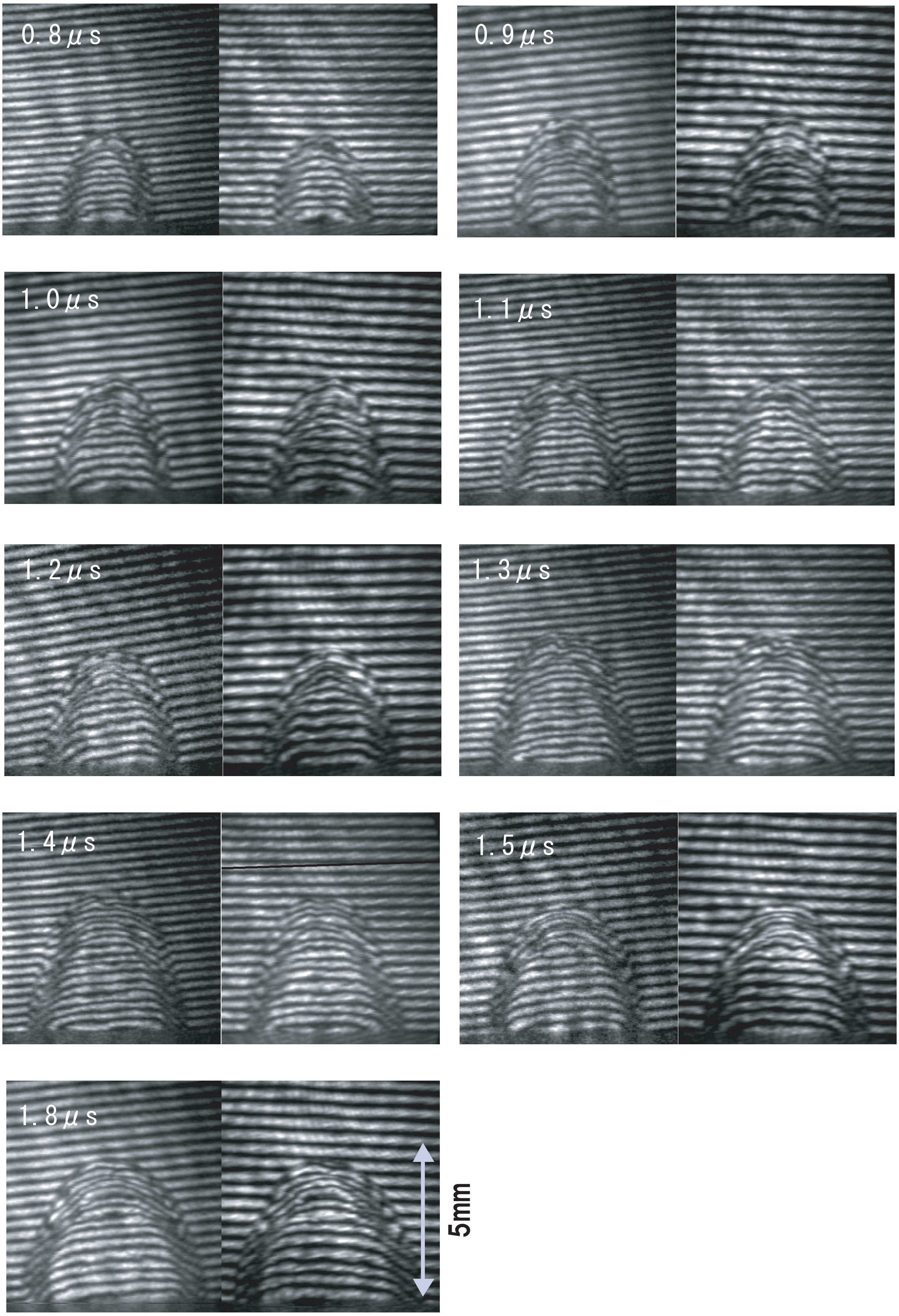

Figure 4.1: Two waverength Mach Zehnder interferograms of the 2D LSD wave (left:532nm right:633nm).

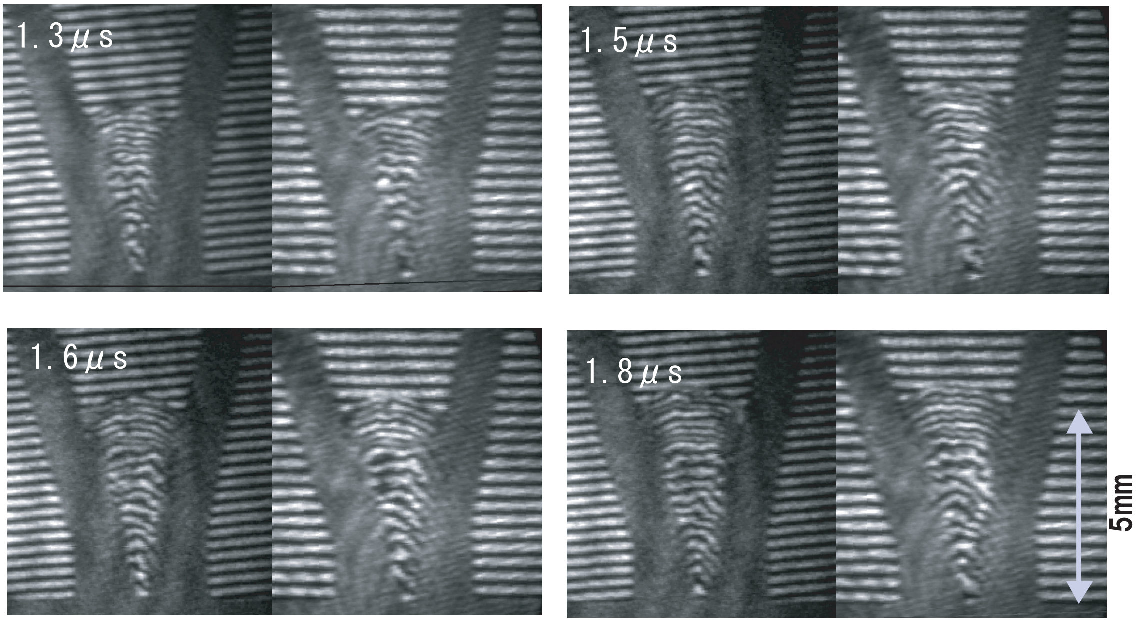

change the projection ratio

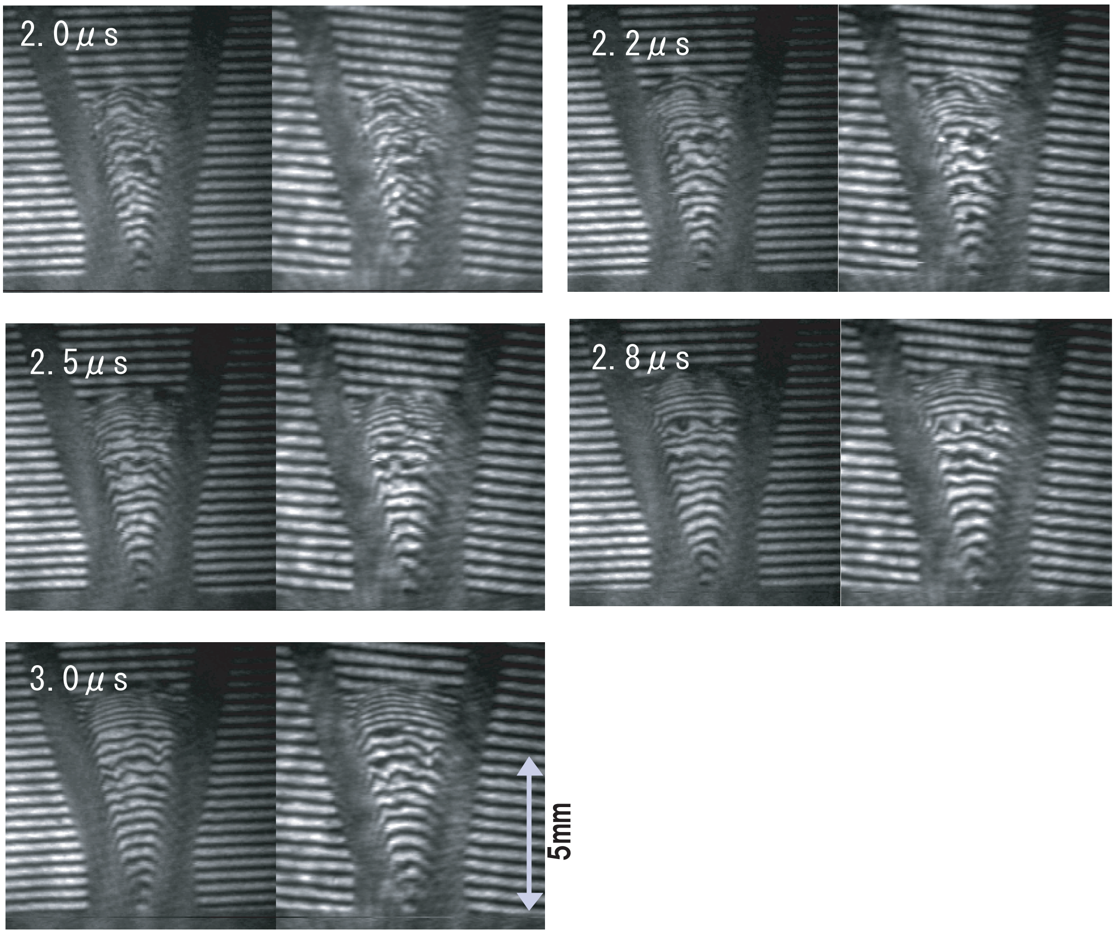

Figure 4.2: Two waverength Mach Zehnder interferograms of the quasi-1D LSD wave (left:532nm right:633nm).

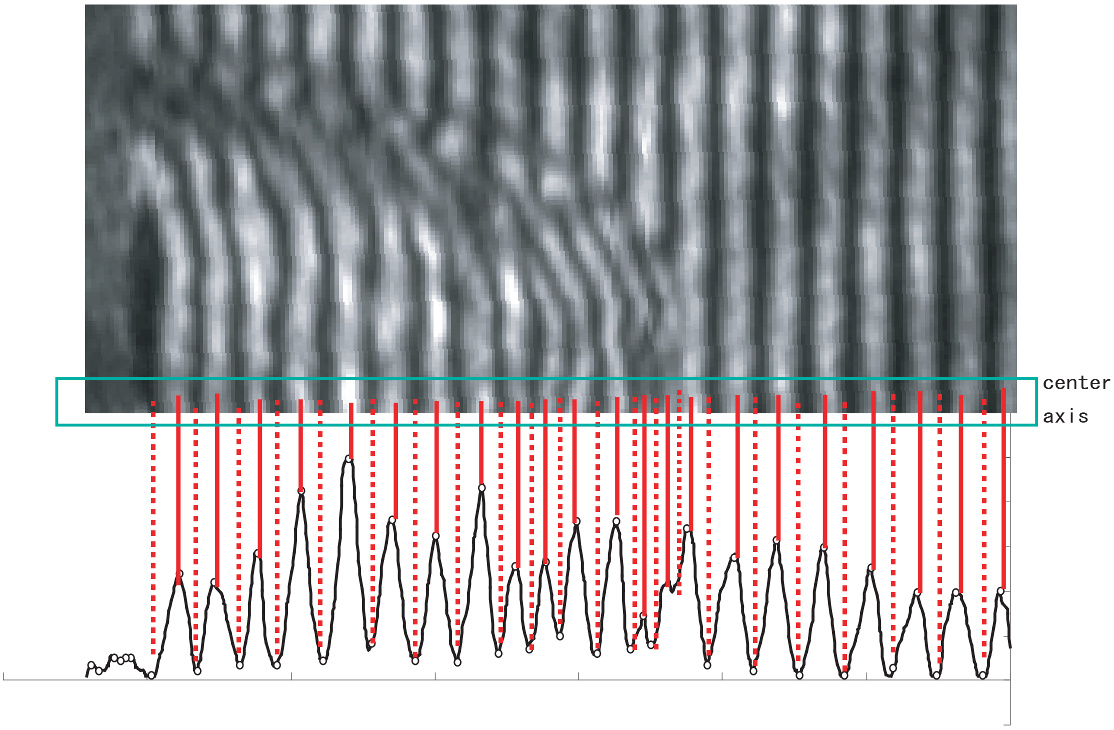

Figure 4.3: The digitalization of the bright and dark on the center axis.

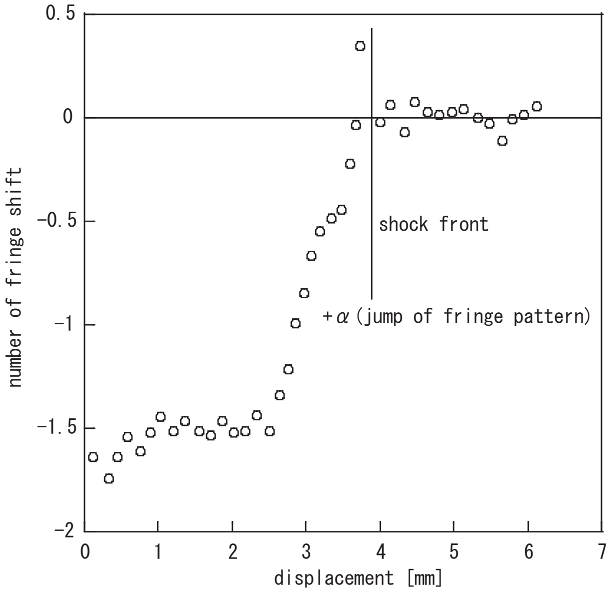

Figure 4.4: Number of fringe shift.

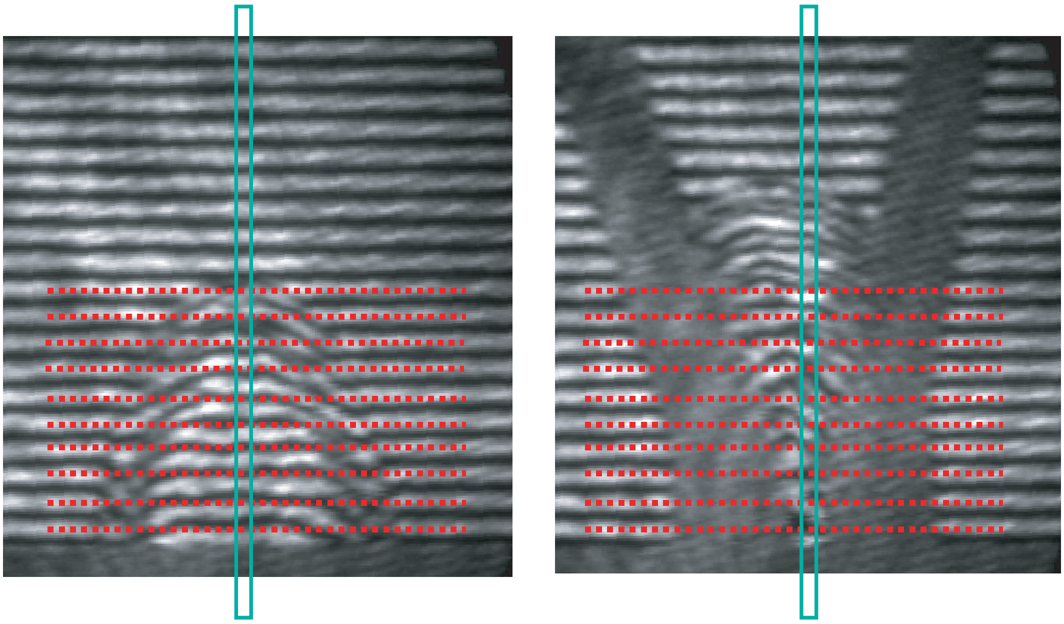

Figure 4.5: Interpolating of the fringe pattern before phenomena on the center axis.

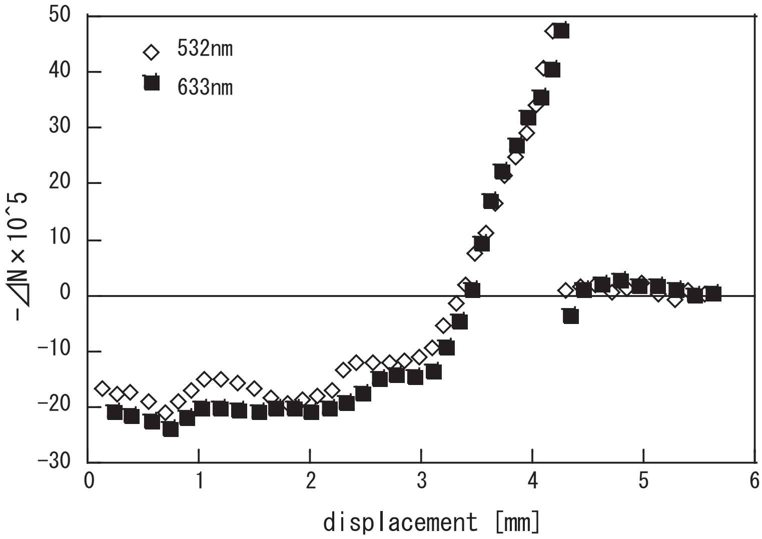

Figure 4.6: the difference of the refractive index.

4.2.3 Calculation of a jump of the fringe pattern on the shock front

The shock front on the center axis is complex phenomena, because laser is irradiated. The otherwise, lateral expansion is untinged from laser, and ascribed conventional shock wave. Therefore using Mach number of lateral expansion, ratio of the density and jump of the fringe pattern is calculated as eq.(2.17),(4.7).

$$\frac{\rho_2}{\rho_1} = \frac{(\gamma+1)M_1^2}{(\gamma-1)M_1^2+2} \tag{4.1}$$

Fig.4.7 shows propagation Mach number in the lateral direction of 2D LSD wave.

However this method is applicable to 2D LSD wave. In quasi-1D LSD wave, there is not lateral expansion. Then in quasi-1D, in distribution of electron, minimum point of this distribution assumes 0 number density.

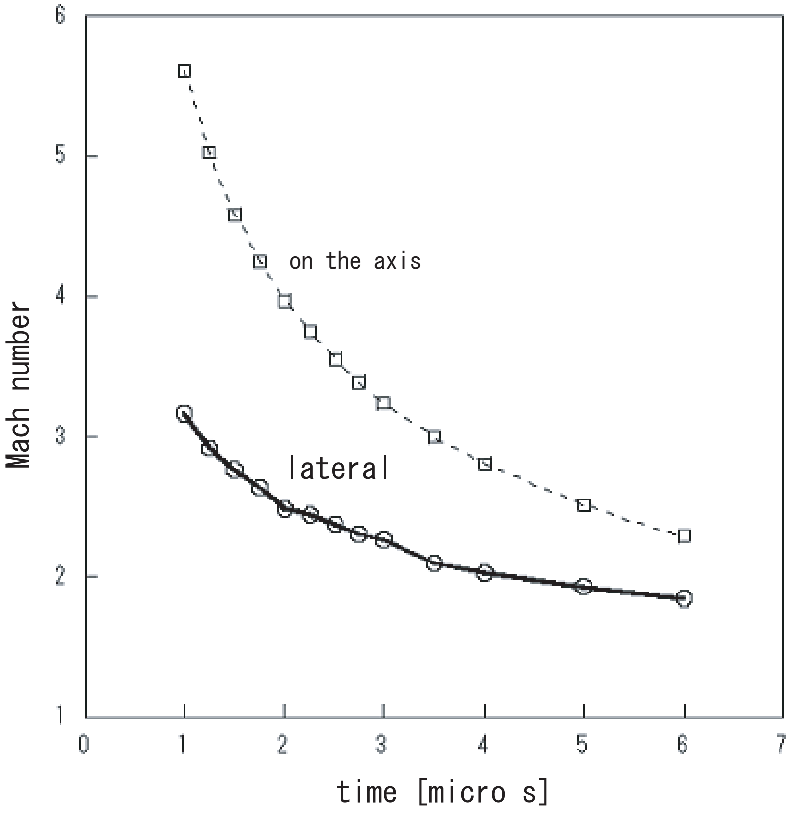

Figure 4.7: Mach number in the lateral dirextion and axial direction in the 2D LSD wave.

4.3 Electron number density distribution

Fig.4.8 and Fig.4.9 shows electron number dnsity distribution of the 2D LSD wave and the quasi-1D LSD wave on the center axis. In these figure, three times experimental result is shown each times. There are peak values of electron density near the shock front. These peak values are separated with time. Especially, this phenomena is occured after LSD termination. Here LSD termination times for 2D and quasi-1D are defined from Shadow Graph experiment as chapter 1-8.

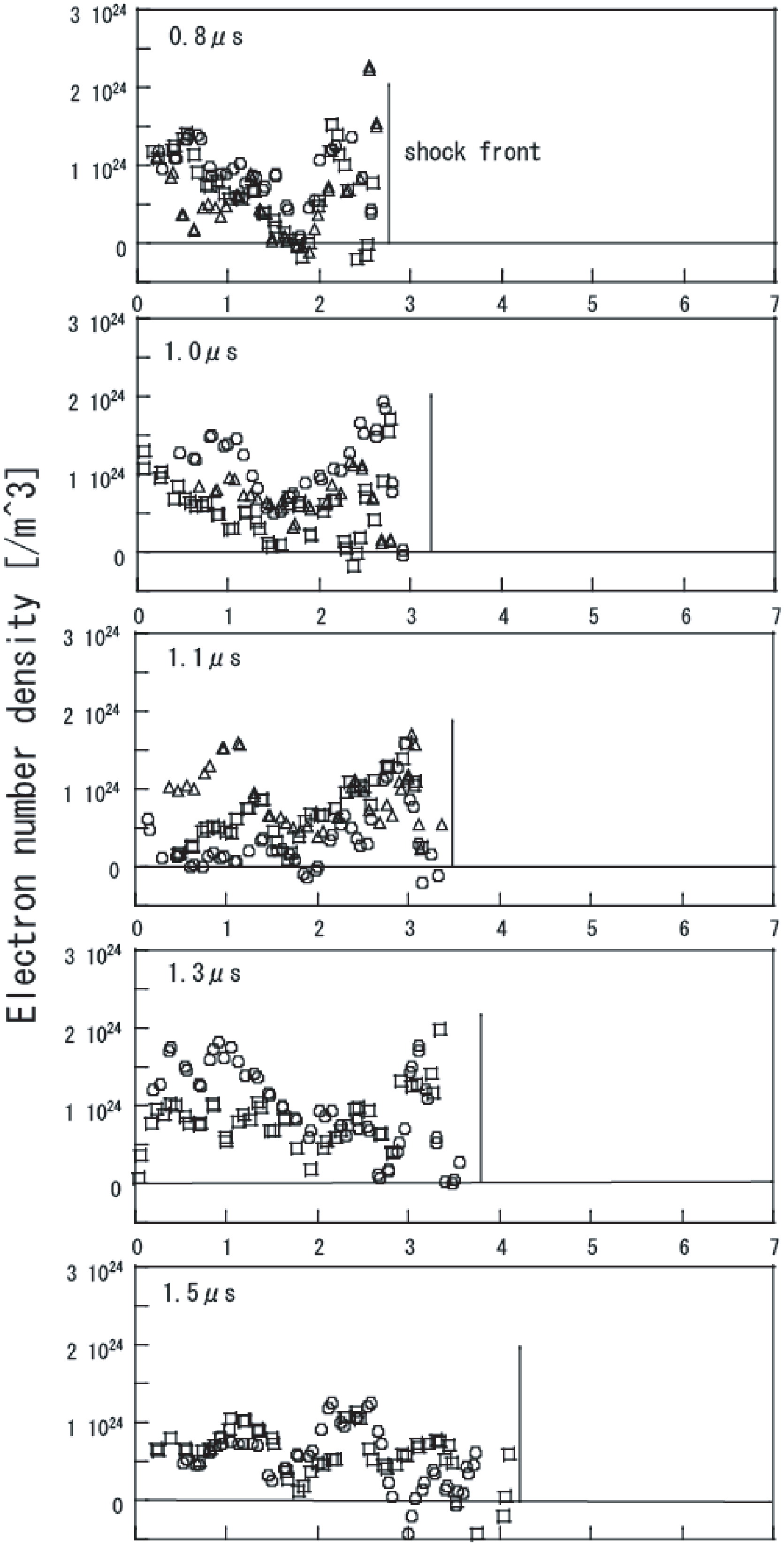

Figure 4.8: Electron number density distribution on the center axis in the 2D LSD wave.

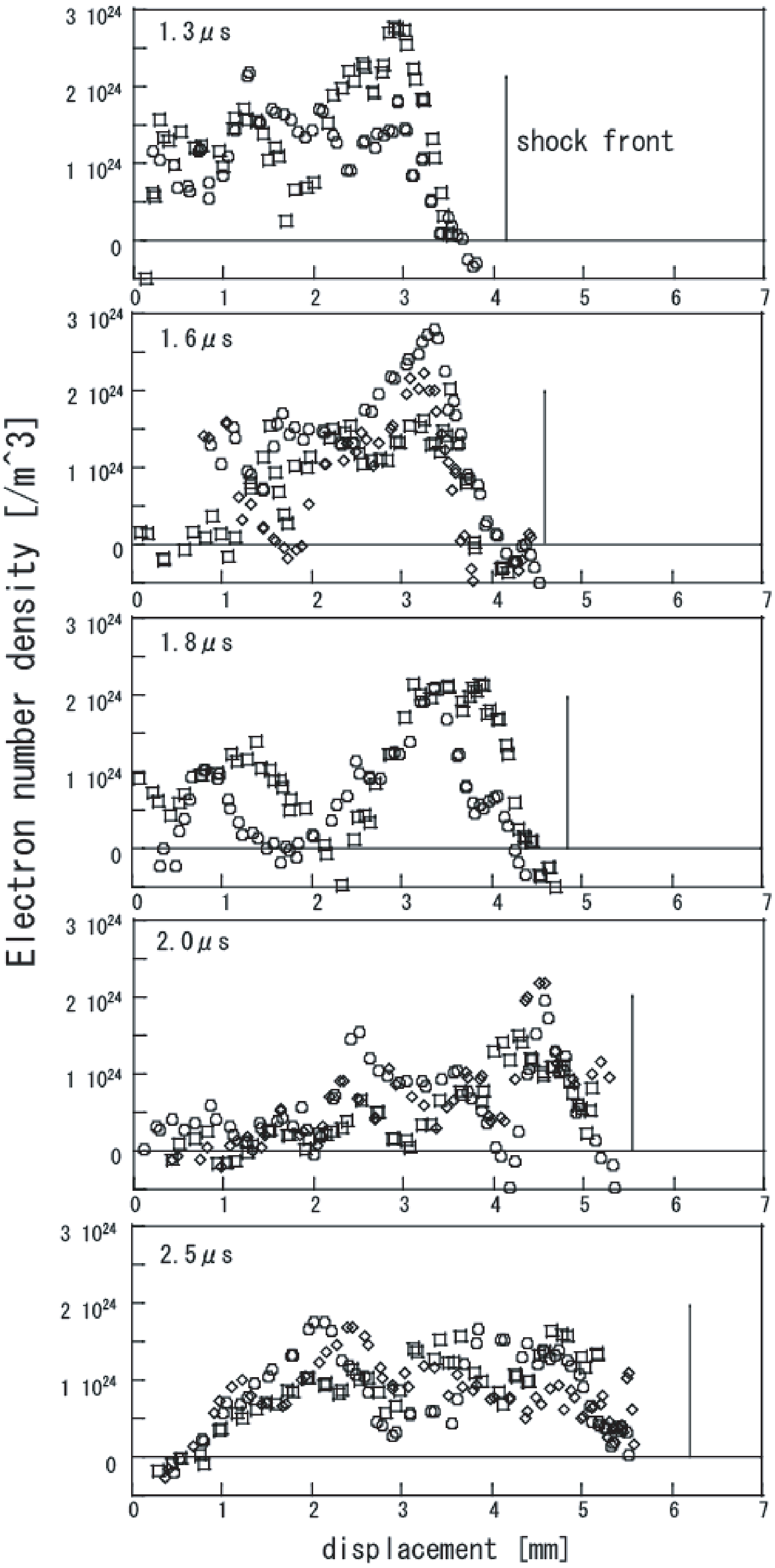

Figure 4.9: Electron number density distribution on the center axis in the quasi-1D LSD wave.

4.4 Discussion

4.4.1 The peak electron density

Figure.4.10 and 4.11 show propagation histories of the shock front and the position of the peak electron density in the 2D-LSD and quasi-1D LSD wave. In these figure, dashed lines are results of Shadowgraph method on the 20mm thick LSD wave. The propagation of the shock front in Mach Zehnder images (2mm thick LSD wave) is well accorded with Shadowgraph images (20mm thick LSD wave). The reason being that laser intensity irradiated on the shock front is same. It is assumed that the time of the LSD termination in 2mm thick LSD wave is accorded with 20mm LSD wave. These times are 1.3μs (2D) and 1.8μs (quasi-1D).

In Fig.4.10 and 4.11, in the LSD regime peak electron density is bordered on the shock front and the propagation speed of the peak position is corresponded with the speed of the shock front. In contrast, after the LSD termination (LSD regime), peak position and shock position are separated. Furthermore, the position of the peak electron density grows stagnant. This difference of the tendency of propagation comes from the difference between LSD regime and LSC regime. In the LSD regime, the construction of the LSD wave (shock + absorption region) is shown from Fig.4.10 and 4.11. In the LSC regime, laser absorption region separated from shock front and formed combustion wave.

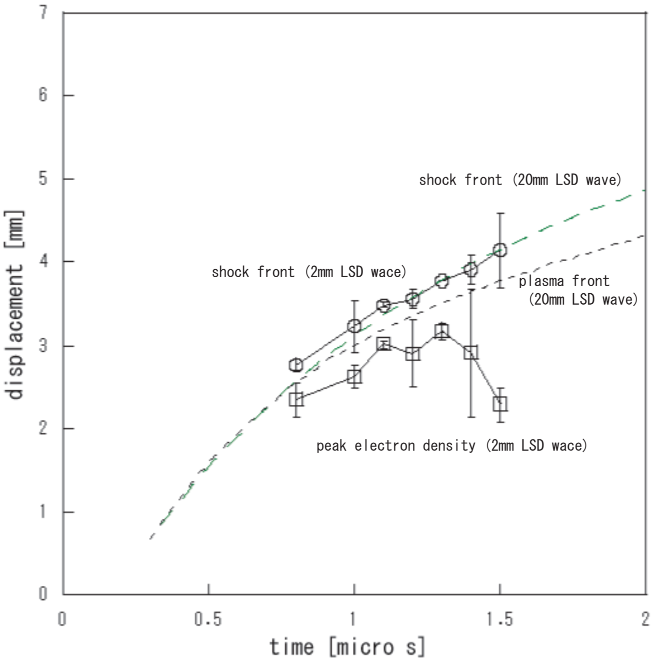

Figure 4.10: The displacement of the shock front and position of the peak electron density in the 2D LSD wave.

Fig.4.12 and shows variation of the peak electron density. The density decreased with time. Especially, near the LSD termination time, gradient of these decreases is shape. Fig.4.13 shows relationship between the laser intensity on the shock front and the peak electron density. In this figure, electron density in the quasi-1D LSD wave is kept the same value in the 2D LSD wave despite laser intensity in quasi-1D case was smaller than 2D case.

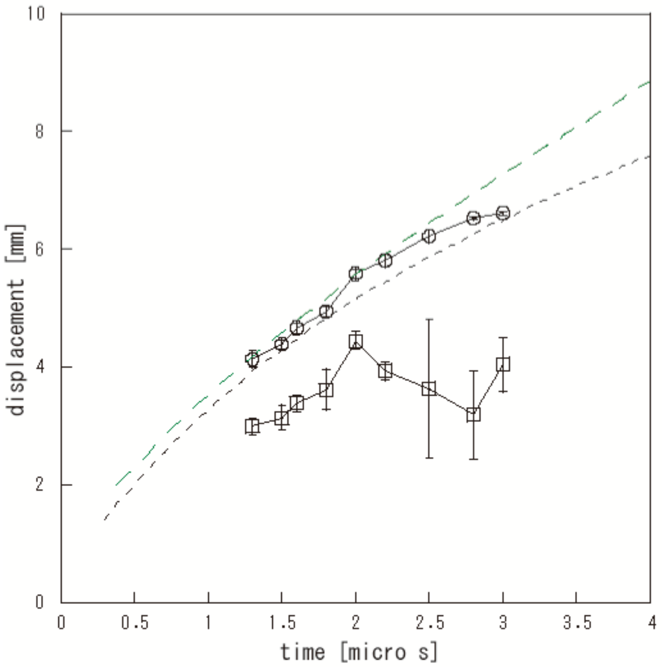

Figure 4.11: The displacement of the shock front and position of the peak electron density in the quasi-1D LSD wave.

Especially, at the LSD termination, the peak value of the electron number density was 1.7~2.0×$10^{24}[m^{-3}]$ in 2D and quasi-1D LSD wave. Despite dimension, velocity and laser intensity are different between 2D and quasi-1D LSD wave, the peak electron number density at the LSD termination was comparable. It is assumed that keeping of 2.0×$10^{24}[m^{-3}]$ peak electron density is one of the important condition for prolong the LSD regime.

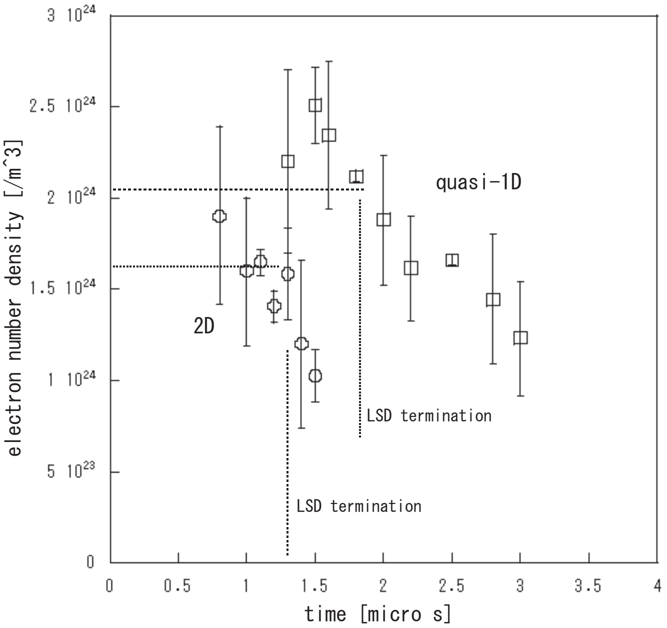

Figure 4.12: Time variation of peak electron density.

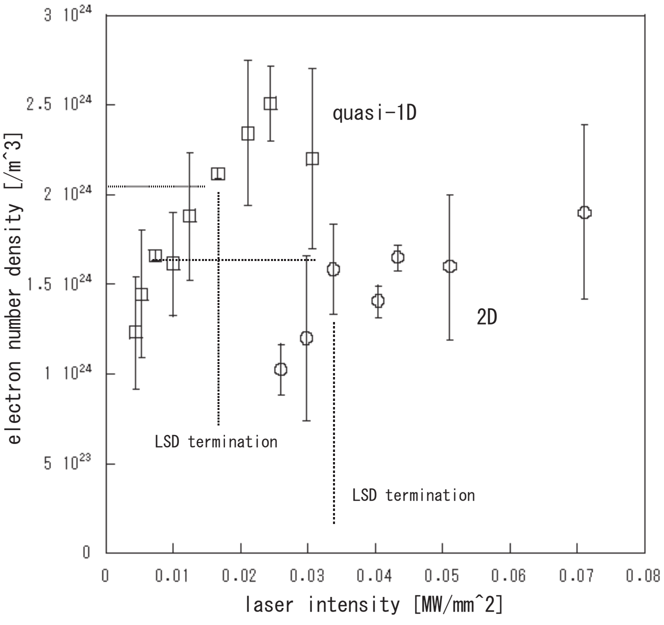

Figure 4.13: Laser intensity variation of peak electron density.

4.4.2 Electron temperature

In these experiments, particle density behind the LSD wave was so high density that LSD wave was generated in atmospheric air. It is considered that LSD wave in this condition is optically thick. And so Local Thermal Equilibrium was assumed. Therefore using saha equation as Eq.(4.2), electron temperature was calculated[23].

$$\frac{N_e N_i}{N_e + N_n} = 2\frac{z_i}{z_n}\frac{(2\pi m_e kT)^{\frac{3}{2}}}{h^3} exp[-U_i/kT] \tag{4.2}$$

Where z_n and z_i is partition functions for neutral and ion, N_e, N_i, N_n the electron, ion, neutral number density, U_i the ionization energy, k the boltzmann constant. In this case,$z_n \cong 4$, $z_i \cong 4$[24]. And $U_i \cong 14.5$ is ascribed the nitrogen ionization energy. Here electron and neutral particle number densitis is necessary to use Eq.(4.2), and electron temperature behind the only 2D LSD wave was estimated.

Fig.4.14 shows time variation of the electron temperature at the position of peak electron density. In this figure, in the LSD regime, electron temperature was about 14000∼14500 [K].

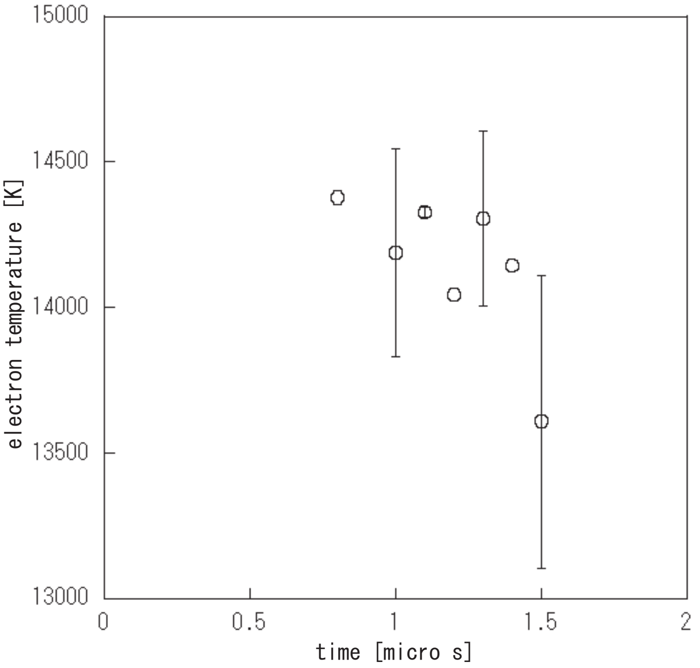

Figure 4.14: time variation of the electron density at the position of the peak electron density.

4.4.3 Absorption length

In the plasma region behind the LSD wave, laser light was absorbed by inverse-bremsstrahlung, which involves the interaction of electron with either ions and neutral particles. The electron-ion absorption coefficient is as follow[25].

$$
\begin{aligned}
k_{e-i} &= \frac{4}{3}G\Big(\frac{2\pi}{3m_e kT}\Big)^{\frac{1}{2}}\frac{z^2e^6\lambda^3}{h_pc^4m_e}n_en_i\big(exp(h_pc/\lambda kT)-1\big) \\
&= 1.37\times10^{-27}G\lambda^3T^{-1/2}n_en_i\big(exp(0.014388/\lambda T)-1\big)
\end{aligned}
\tag{4.3}
$$

Where λ is laser wavelength, e the electron charge, c the speed of light, m_e the electron mass and h_p Plank’s constant. To account for quantum-mechanical effects, Eq.(4.3) was multiplied by a Gaunt factor G. Here G is fitted $G = 1.04 + 3.74 \times 10^{-5}T - 3.28 \times 10^{-10}T^2$

In otherwise, electron-neutral particles absorption coefficient is as follow[25].

$$
\begin{aligned}
k_{e-n} &= \frac{k^2T^2A(T)\lambda^3}{h_pc}n_en_n\big(1-exp(-h_pc/\lambda kT)\big) \\
&= 9.6\times10^{-5}T^2A(T)\lambda^3n_en_n\big(1-exp(-0.014388/\lambda T)\big)
\end{aligned}
\tag{4.4}
$$

Where factor $A(T)$ is taken from reference[25]. From Eq.(4.3) and (4.4), absorption length l was estimated as follow

$$
l = \frac{1}{k_{e-i}+k_{e-n}} \tag{4.5}
$$

Fig.4.15 shows the time variation of absorption length for the CO_2 laser. From this figure, in the LSD regime, absorption length was about 0.1~0.2mm. This length lengthens with time, because electron number density went down. From Eq.(4.3) and (4.4), absorption length is most influenced on electron density.

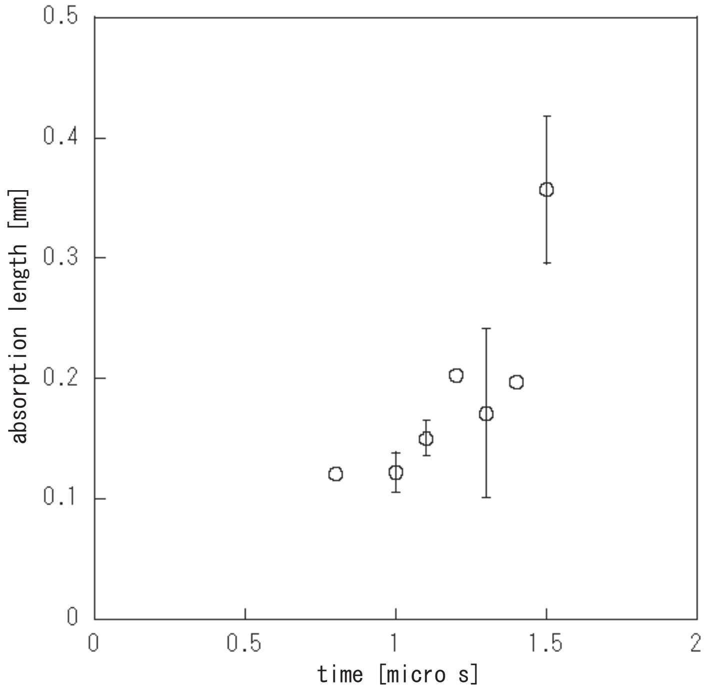

Figure 4.15: time variation of the absorption length at the position of the peak electron density.

Chapter 5

Conclusion

- The electron number density distribution behind the 2D and quasi-1D LSD wave was measured. In the LSD regime, the propagation speed of the peak position of the electron density was similar to the shock speed. In otherwise, after the LSD termination, the peak position grew stagnant and the electron distribution was changed gentle declivity with time.

  The peak value of the electron density was decreased with time. The electron density in the quasi-1D LSD was comparable to the density of the 2D LSD wave despite low laser intensity.

  Especially, at the LSD termination, the peak value of the electron number density was $1.7\sim 2.0\ \times 10^{24}$ in 2D and quasi-1D LSD wave. Despite difference of dimensions, propagation velocities and laser intensity between 2D and quasi-1D LSD wave, the peak electron number density at the LSD termination is about the same. It is assumed that keeping of 2.0 $10^2$4 peak electron density is one of the important condition for prolong the LSD regime.

- About 2D LSD wave, electron temperature was estimated using saha equation under the local thermal equilibrium. In LSD regime, this temperature of the position of peak electron density was

  14000∼14500 [K]

  From the electron temperature, absorption length at the electron peak position was estimated

  0.1∼0.2 [mm]

  This absorption length lengthens with time. And this length is quite shorter than plasma existence region.

Bibliography

[1] Kantrovitz, A. "Propulsion to Orbit by Ground Based Lasers," *Aeronautics and Astronautics*, vol.10, 1972, pp. 74-76.

[2] Hettche, L. R., Schriempf, J. T., and Stegman, R. L., "Impulse reaction resulting from the in-air irradiation of aluminum by a pulsed CO_2 laser," *Journal of Applied Physics*, Vol. 44, 1973, pp. 4079-4085.

[3] Pirri, A. N., Schler, R., and Northam, D., "Momentum transfer and plasma formation above a surface with a high-power CO_2 laser," Applied Physics Letters, Vol. 21, 1972, pp. 79-81.

[4] Simons, G. A., "Momentum Transfer to a Surface When Irradiated by a High-Power Laser," *AIAA Journal*, Vol. 22, 1984, pp. 1275-1280.

[5] Simons, G. A., and Pirri, A. N. "The Fluid Mechanics of Pulsed Laser Propulsion," *AIAA Journal*, Vol.15, 1977, pp. 835-842.

[6] Pirri, A. N., and Monsler, M. J., "Propulsion by Absorption of Laser Radiation," *AIAA Journal*, Vol. 12, 1974, pp. 1254-1261.

[7] Ageev, V. P., Barchukov, A. I., Bunkin, F. V., Konov, V. I., Korobeinikov, V. P., Putjatin, B. V., and Hudjakov, V. M., "Experimental and theoretical modeling of laser propulsion," *Acta Astronautica*, Vol. 7, 1980, pp. 79-90.

[8] Bohn, W. L. "Laser Lightcraft Performance," *Proceedings of SPIE*, Vol. 3885, 2000, pp. 48-53.

[9] Myrabo, L. M., Messitt, D. G., and Mead, Jr., F. B., "Ground and Flight Tests of Laser Propelled Vehicle," *AIAA Paper* 98-1001, 1998.

[10] Sasoh, A., "Laser-Propelled Ram Accelerator," *Journal of Physics IV France*, Vol.10, 2000, pp.41-47.

[11] katsurayama, H., komurasaki, K.,Momozawa, A., and Arakawa, Y., "Numerical and Engine Cycle Analysis of a Pulse Laser Pamjet Vehicle," *Transaction of JSASS Space Technology Japan*, Vol.1, 2003, pp.9-16.

[12] Zel'dovich, Y. B., and Raizer, Yu. P., "Physics of Shock waves and High-temperature Hydrodynamics Phenomena," Dover, NewYork, 2002,

[13] Raizer,Y.P., "Laser-Inducede Discharge Phenomena," pp.199-204, 1972.

[14] Fischer, V. I., Soviet Physics: Technical Physics, Vol.28, 1984.

[15] Jumper, E. J., *Physics of Fluids*, Vol.21, 1978, p. 549.

[16] Nielsen, P. E., "Hydrodynamic calculations of surface response in the presence of laser-supported detonation weaves," *Journal of Applied Physics*, Vol. 46, 1975, pp. 4501-4505.

[17] Kazuyasu, M., "Compressible Flow Dynamics," *Rikougakusha*, p184, 1994.

[18] Batenin, V. M., Klimovskii, I. I., Lysov, G. V. and Troitskii, V. N, "Superhigh Frequency of Plasma," *CRC Press,Inc*, 2000.

[19] Hiroyuki, S., "Numerical Analysis of Generation and Propagation Mechanism of Laser-supported Detonation in Argon Gas," *Doctor thesis, the university of Nagoya*, 2000.

[20] K, Mori. K, Komurasaki., *Journal of Applied Physics*, Vol. 92, 2002 pp. 5663

[21] 村岡克紀, 前田三男"プラズマと気体のレーザー応用計測" 産業図書 (1995).

[22] Richard H. Huddlestone and Stanley L. Leonard "Plasma Diagnostic Techniques" Academic Press, New York(1965).

[23] Manabu, Yamamoto. seiichi, Murayama., "プラズマの分光計測," 日本分光学会測定法シリーズ, 1996.

[24] NIST Atomic Spectra Database http://physics.nist.gov/PhysRefData/ASD/index.html

[25] N. H. Kemp, P. F. Lewis, "Laser -Heated Thruster - Interim Report" *Pyhsical Science Inc*, 1 Sep. 1978 - 31 Aug. 1979 pp. 178

Conference and Paper

- Confernece
  - 平成17年度 宇宙輸送シンポジウム　神奈川, 1月, 2006
    "線状集光レーザー支持デトネーション波(LSD波)のエネルギー変換過程の研究"
  - 第26回 レーザー学会学術講演会年次大会　大宮, 2月, 2006
    "レーザーの線状集光によるレーザー支持デトネーション波背後のエネルギー変換過程"
  - 衝撃波シンポジウム　神奈川, 3月, 2006
    "レーザー支持デトネーション波背後の電子密度分布"
  - 25th International Symposium on Space Technology and Science Kanazawa, June, 2006
    "Electron Number Density Behind a Laser Supported Detonation Wave"
  - 平成18年度 宇宙輸送シンポジウム　神奈川, 1月, 2006
    "準1次元レーザー支持デトネーション波背後の電子密度測定"
- Paper
  - Journal of the Combustion Sciety of Japan Vol. 48 No. 146 (2006) 323-327
    "レーザー支持爆轟と爆風波へのエネルギー変換"